2001

Iterative blind deconvolution and its application in characterization of eddy current NDE signals

Xiang Cai
Iowa State University

Iterative blind deconvolution and its application in characterization of eddy current NDE signals

Xiang Cai

Major Professor: Dr. Lalita Udpa
Iowa State University

Eddy current techniques are widely used to detect and characterize the defects in steam generator tubes in nuclear power plants. Although defect characterization is crucial for the successful inspection of defects, it is often difficult due to due to the finite size of the probes used for inspection. A feasible solution is to model the defect data as the convolution of the defect surface profile and the probe response. Therefore deconvolution algorithms can be used to remove the effect of probe on the signal.

This thesis presents a method using iterative blind deconvolution algorithm based on the Richardson – Lucy algorithm to address the defect characterization problem. Another iterative blind deconvolution method based on Wiener filtering is used to compare the performance. A preprocessing algorithm is introduced to remove the noise and thus enhance the performance. Two new convergence criterions are proposed to solve the convergence problem. Different types of initial estimate of the PSF are used and their impacts on the performance are compared. The results of applying this method to the synthetic data, the calibration data and the field data are presented.

Iterative blind deconvolution and its application to characterization of eddy current NDE signals

by

Xiang Cai

A thesis submitted to the graduate faculty

in partial fulfillment of the requirements for the degree of

MASTER OF SCIENCE

Major: Electrical Engineering

Major Professor: Dr. Lalita Udpa

Iowa State University

Ames, Iowa

2001

Graduate College

Iowa State University

This is to certify that the Master's thesis of

Xiang Cai

has met the thesis requirements of Iowa State University

Major Professor

For the Major Program

For the Graduate College

TABLE OF CONTENTS

LIST OF FIGURES

LIST OF TABLES

ACKNOWLEDGEMENTS

I would like to express my grateful appreciation to my major advisor Dr. Lalita Udpa for her continuous guidance and encouragement during my graduate study at Iowa State University. Her immense knowledge of the subject with excellent abilities as a teacher has been a source of inspiration.

I am also deeply indebted to Dr. Satish Udpa and Dr. Joseph Gray for their valuable advice and comments as members of my graduate committee.

During the completion of this research work, I benefited from many interesting and enlightening discussions with my colleagues and friends in Ames, Iowa. My special thanks go to Nawapak Eua – Anant, Pradeep Ramuhalli, Zhiwei Zeng, Ping Xiang, and Liang Xuan.

Appreciation is also extended to FAA. Their continuous support and help throughout the past three years are gratefully acknowledged.

Last but certainly not the least, I would like to thank my parents for their guidance, support and encouragement throughout my education. I owe both of them a great deal.

This work was performed at Ames Laboratory under Contract No. W-7405-Eng-82 with the U.S. Department of Energy. The United States government has assigned DOE Report number IS-T 2183 to this thesis.

ABSTRACT

Eddy current techniques are widely used to detect and characterize the defects in steam generator tubes in nuclear power plants. Although defect characterization is crucial for the successful inspection of steam generator tubes, it is often rendered difficulty due to the artifacts introduced by the finite size of the probes used for inspection. A feasible solution is to model the data as a convolution of the defect surface profile and the probe response and use deconvolution algorithms to remove the effect of probe on the signal.

This thesis presents study of a iterative blind deconvolution technique based on the Richardson – Lucy algorithm to address the defect characterization problem. The performance is compared with results obtained using iterative method based on Wiener filtering. A preprocessing algorithm is introduced to remove the noise and thus enhance the performance. Two new convergence criterions are proposed to enhance the solution. Different types of initial estimate of the PSF are used and their impact on the performance is studied. Results of applying this method to synthetic data, calibration data and field data are presented.

CHAPTER 1. INTRODUCTION

1.1 Problem Statement

Nondestructive evaluation (NDE) is the inspection and evaluation of a test material for defects without causing any damage to the properties and serviceability of the specimen. NDE techniques are widely used in a variety of industrial applications, especially in the area of detecting and characterizing flaws in engineering structures such as airplane wheels and engines, bridges, gas pipes, railroads, nuclear power plants and so on. Defects, which are mostly cracks caused by intensive workload or extreme environmental conditions, can cause fatal failures with disastrous consequences. Timely and successful detection of such defects can certainly lead to decreasing the possibility of failure and increasing the quality of service.

A variety of nondestructive testing (NDT) methods including electromagnetics, ultrasonics, radiography, and thermography, have evolved to handle a large variety of applications. A typical NDT system consists of three components: a specimen under inspection, an energy source that interacts with the specimen, and a receiving transducer to pick up the response of energy – material interaction. For example, acoustic waves are used in ultrasonic methods of testing, and X – rays are used as the source of energy in radiographic techniques. A typical NDT signal consists of the response of energy – material interaction. For instance, examples of electromagnetic NDT signals include magnetic flux leakage, potential drop, and impedance changes of an eddy current coil.

Such NDT signals can be further analyzed using different signal/image processing techniques to obtain useful information, such as location, shape, and depth, of the defects.

One of the most commonly used electromagnetic inspection techniques is eddy current method that is widely used in aerospace, automotive, marine and manufacturing applications for detection and characterization of flaws in conducting, ferromagnetic and non – ferromagnetic materials. This method is based on measuring the changes of the probe coil impedance as the probe scans the surface of a conducting specimen. These changes may indicate either the presence of a defect on the specimen, or material property variation of the specimen.

One of the major applications of eddy current method is in the inspection of the steam generator tubes in nuclear power plants [1]. In this application, the overall eddy current testing system can be roughly divided into two parts: the measurement system that is used to collect eddy current NDT signals, and data analysis system that is used to extract useful information about the defect. The main objective of signal/image processing algorithms used in data analysis system is defect characterization. Defect characterization refers to determining the defect parameters such as shape, length, width, and depth from the information contained in eddy current signals. Defect characterization can be further decomposed into 2 parts: 1) estimating the surface profile of the defect; 2) reconstruct the depth profile. Together a three – dimensional defect reconstruction can be performed.

In general it is seen that eddy current signals extend beyond the surface extent of a defect. In step (1) this problem can be addressed by assuming the signal is a convolution

of the defect footprint (the surface profile of the defect) and the probe response. Therefore, deconvolution algorithms [2] can be applied to remove the effects of the probe on the signal and give a better estimate of the true defect dimensions. An additional advantage of deconvolution is that it can separate out two or more flaws in close proximity, thus better characterizing the true nature of the flaw.

Most deconvolution algorithms require a priori knowledge of the probe response or the kernel function. This parameter, though vital for improving the performance of the algorithm, is often hard to obtain. A simple approach to deconvolution is based on the use of Wiener filters [3], where the form of the kernel is assumed. Blind deconvolution algorithms [2, 4] are better suited in applications where the form of the kernel function is unknown and must be estimated from the data at hand. The major advantage of blind deconvolution algorithms over other deconvolution algorithms is that the probe response and defect footprint can be estimated sequentially from the defect signals. Another advantage is that additional constraints can be easily incorporated into the deconvolution process, thus resulting in improved characterization results.

1.2 Scope of Thesis

This thesis deals with the problem of defect characterization using blind deconvolution techniques. The technique discussed in this thesis is based on one of the commonly used blind deconvolution algorithm, Richardson – Lucy algorithm [5, 6]. Although blind deconvolution techniques are often used in image restoration applications, it can also be used to address the defect characterization problem due to

similarity of the image degradation system and the eddy current inspection system. The Richardson – Lucy algorithm was derived from Bayes's theorem, and it models the input image, kernel function, and observed image as probability – frequency function. Due to its implementation of maximum likelihood and ability to reconstruct input images with high quality even under noisy conditions, it has been widely used in a variety of problems.

This thesis is organized as follows:

Chapter 2 introduces the different types of nondestructive testing techniques and gives a brief description of the theory of the eddy current method. This chapter also includes the description of the measurement system used to inspect the steam generator tubes in nuclear power plants. In addition, a description of data analysis system including data preprocessing and signal enhancement and the challenge of obtaining better characterization results is included.

Chapter 3 gives an overview of two different types of blind deconvolution algorithms: parametric and non – parametric. Several commonly used blind deconvolution algorithms and their advantages and disadvantages are discussed in this chapter.

Chapter 4 first gives a detailed review of the blind deconvolution method based on Richardson – Lucy algorithm along with the implementation of the eddy current signals is explained. Modifications that are made to make the algorithm more suitable for dealing with the eddy current signals are also discussed.

Chapter 5 shows the results of Richardson – Lucy based blind deconvolution method applied to the eddy current signals obtained from the steam generator tubes in nuclear power plants. Both calibration data and field data are used to evaluate the performance of the algorithm. Also included in this chapter are some concluding remarks and identification of areas for future research.

CHAPTER 2. EDDY CURRENT NDE

2.1 Introduction

A typical NDT system is shown in Figure 2.1[7]. The receiving transducer is used to pick up the interaction between the energy source and the test specimen and thus generate an output signal. The output signal is then processed and passed through an inverse block that analyzes the signal measured by the receiving transducer. In the last step a defect characterization technique is used to predict an estimate of the defect profile.

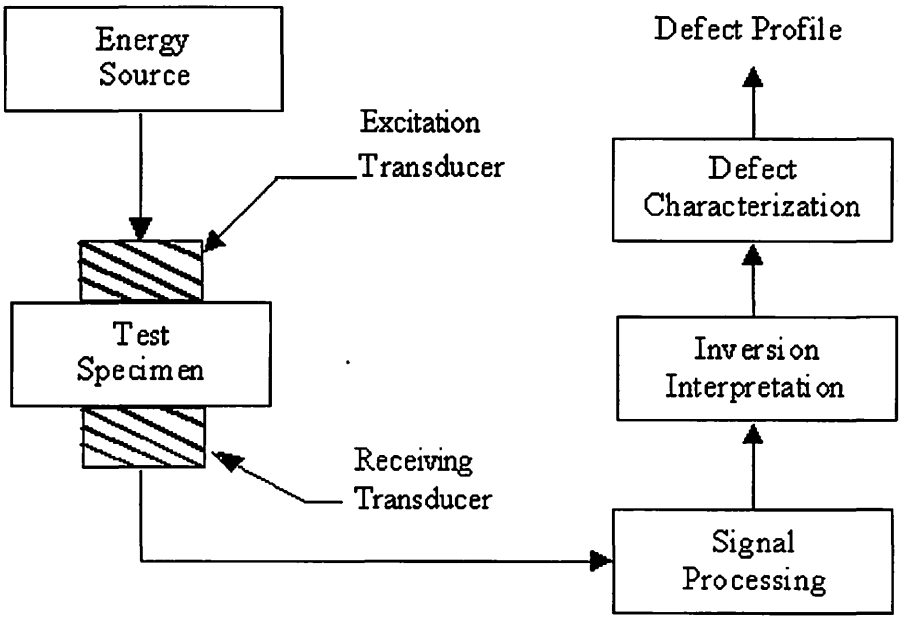

Figure 2.1 A general NDT system

2.2 General Methods of Nondestructive Testing

Currently a variety of nondestructive testing methods are in existence and they are classified according to the types of probing energy source used. Three of the most commonly used NDT methods are ultrasonic, radiographic, and eddy current methods which are described next.

2.2.1 Ultrasonic NDT

The ultrasonic method is probably one of the oldest NDT methods. It belongs to the family of acoustic nondestructive inspection techniques which utilize characteristics of the propagating stress waves [8]. These waves are generally in the ultrasonic range, i.e., having frequencies greater than 20 kHz. Hence, it is called the ultrasonic NDT. This method needs to inject a burst of energy in ultrasonic frequency range into the test specimen through a transducer. The injected ultrasonic wave passes through the specimen and interacts with the material. The return echo is picked up by a receiving transducer and this echo carries information about the property of the material along the path the ultrasonic wave travels.

A general ultrasonic testing system is shown is Figure 2.2 [9]. A pulse generator generates the electrical pulses, a transducer converts electrical pulses into mechanical waves, a receiving transducer collects the echoes from the test specimen, and a display and analysis system. Depending on the mode of operation, either one or two transducers can be used [10].

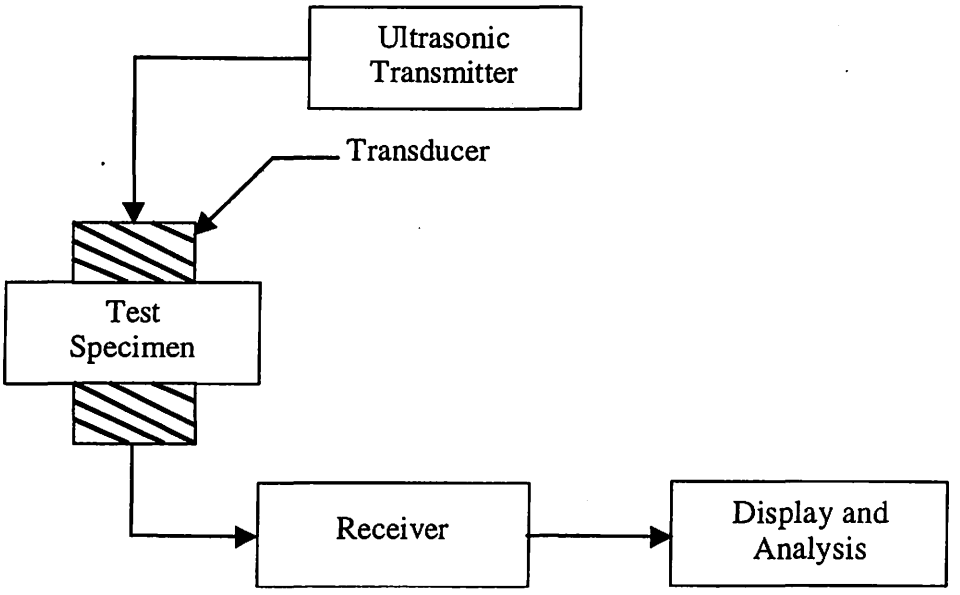

Figure 2.2 A general ultrasonic inspection system

There are three typical modes of displaying the data, namely, A – scan, B – scan and C – scan. In A – scan mode, the echoes of the output signal is recorded as a one – dimensional function of time for a given position of the transducer and provides information of the depth of the defect. The B – scan signal consists of a series of A – scan signals obtained with the transducer scanning along the length of the test specimen thereby providing a cross – sectional view of the defect shape. The C – scan consists of a set of B – scan signals, in which the transducer performs a 2 – D scan of the surface of the test specimen, and the peak value of the A – scan at each position is displayed. The display and analysis system implements post – processing techniques for extracting the

useful information to either determine the size and location of the flaw or measure the properties of the material.

2.2.2 Radiographic NDT

Radiography method was the first NDT method used for inspecting samples for internal defects. It is widely used for finding internal, nonplanar defects such as porosity and voids. But planar defects can also be located with radiography if properly oriented. It is also suitable for detecting changes in material composition, for thickness measurement, and for locating unwanted or defective components that can not be seen in assembled parts.

Radiographic NDT method is based on propagation of energy from a source through an object and analysis of the energy pattern received on the opposite side. Figure 2.3 shows a typical radiographic inspection system. The radiation source used can be X – rays or gamma rays which emit energy that travels in straight lines and penetrates the test specimen. Both sources are electromagnetic radiation of high frequencies with wavelength of the order of 10^{-7} to 10^{-11} cms. Gamma rays are generated by transition of a radioactive nuclei from a high energy level to a more stable lower energy level, and x – rays are produced when high – speed electrons strike a suitable target [8]. Because of the high energy level the radiation has high penetrating power and can travel through most materials. The intensity of the beam of energy transmitted through the object is reduced according to the thickness traversed by the beam and can be expressed as:

$$I_t = I_0 e^{-\lambda t} \tag{2.1}$$

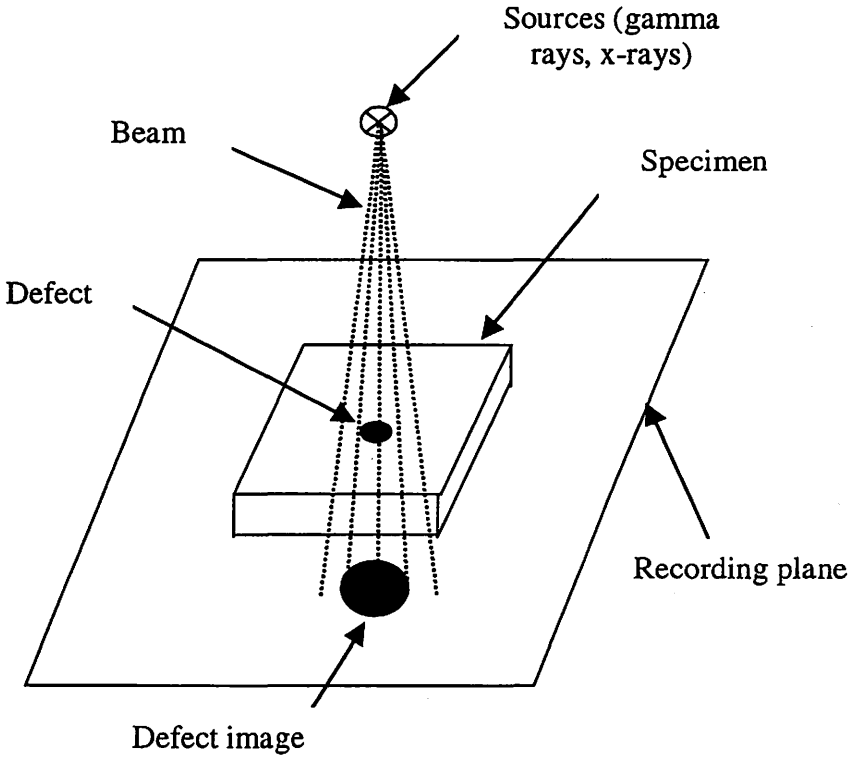

Figure 2.3 A general radiographic inspection system [8].

where t is the thickness of the material, I_0 and I_t are the incident and transmitted energies respectively, and λ is the linear absorption coefficient dependent on the material properties. After the radiation energy has passed through the test specimen, it is recorded on a photographic film opposite the source and analyzed to determine the condition of the test specimen.

2.2.3 Electromagnetic NDT

In electromagnetic NDT methods, the energy source is electric and magnetic fields. Some of the popular electromagnetic methods are potential drop, magnetostatic leakage field, and eddy current methods. The magnetic leakage field technique uses direct current as the excitation source, while the eddy current method uses a low frequency alternating current. The magnetic field is varied because of the variation of one or more properties such as magnetic permeability, electric permittivity or electric conductivity of the test specimen. Excitation current also has an impact on the generated magnetic field. The NDT technique used in this thesis is based on the eddy current method. Eddy Current methods are one of the most popular nondestructive testing techniques and are widely used in the inspection of aircraft and nuclear power plants. The physical principles of this method are described in the following sections.

2.3 Principle of Eddy Current Testing

Eddy current methods are based on the principles of magnetic induction to interrogate the tested specimen [6, 11, 12, 13].

When a coil is excited by an alternating current, a primary magnetic field that is parallel to the coil's axis is generated. According to Faraday's laws, when this coil is brought close to a conductive specimen eddy current is induced in the specimen. Hence, a secondary magnetic field is generated due to the presence of the induced eddy currents in the specimen. From Lenz's law, the direction of the induced eddy current and the

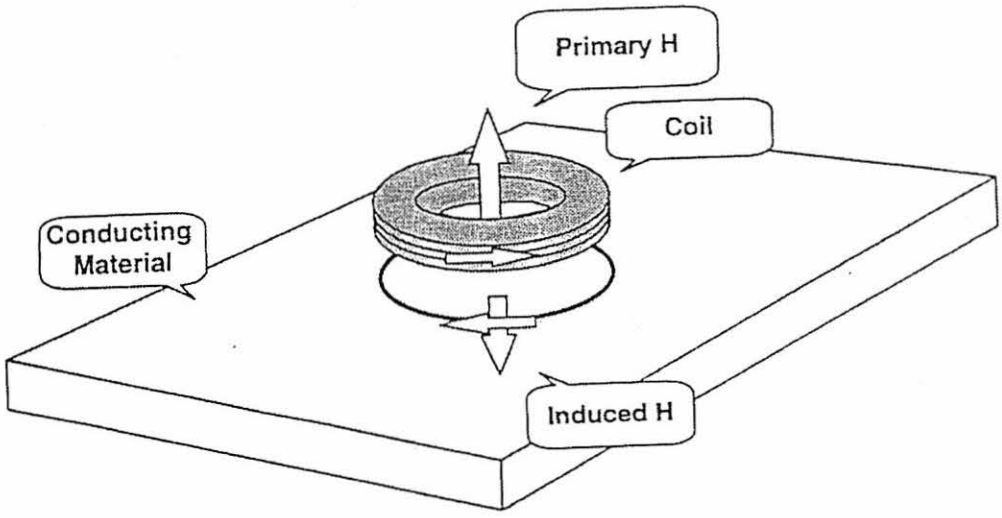

Figure 2.4 Principles of Eddy Current Testing [7]

secondary magnetic field has the tendency to oppose the primary magnetic field. Figure 2.4 illustrates the principles of eddy current testing.

If the specimen is nonferromagnetic, the flux linkage of the primary field is decreased because the secondary field opposed the primary field. Since the self – inductance of the coil is proportional to the flux linkage, the inductance of the coil is decreased. At the same time, the resistance of the coil is increased because the eddy current losses occurred in the specimen have to be compensated by the source of excitation.

In the presence of a flaw or defect in the test specimen, the distribution of the induced current is changed. The eddy current is reduced due to the presence of the discontinuity or inhomogeneity in the material. The change of induced eddy current results in the reduction of the changes of the inductance and resistance of the excitation coil. Figure 2.5 shows the changes of the inductance and resistance of the excitation coil

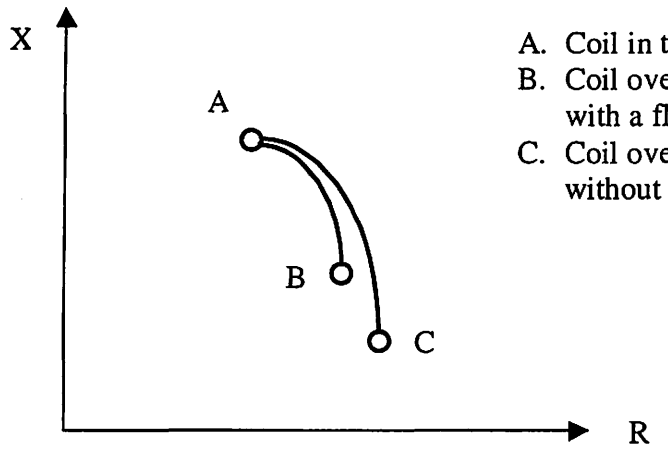

Figure 2.5 Impedance plane trajectory of a coil over a nonferromagnetic specimen.

in the presence and absence of a defect in the test specimen under assumption that the specimen is nonferromagnetic [11].

When the test specimen is ferromagnetic, the change of inductance of the excitation coil is different. Besides the reduction of the inductance of the coil due to the effect of the induced eddy current in the test specimen, the higher permeability of the material results in an increase in the inductance of the coil. Generally, the latter effect is stronger and, hence the net inductance is increased in the case of ferromagnetic specimen. The change in the resistance of the coil is the same as in the case of a nonferromagnetic specimen. Figure 2.6 [11] illustrates the changes of inductance and resistance of the excitation coil in the presence and absence of a defect in the ferromagnetic specimen.

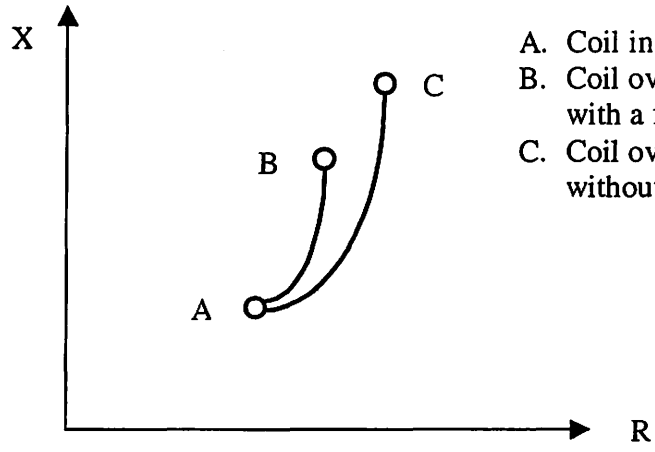

Figure 2.6 Impedance plane trajectory of a coil over a ferromagnetic specimen.

2.4 Eddy Current Transducer

Eddy current transducers can be divided into different classes according to coil configuration [11]:

1. absolute eddy current transducers;
2. differential eddy current transducers;
3. absolute and differential eddy current array transducers;

Absolute eddy current transducers usually consist of a single coil. When using absolute transducers, the absolute value of the impedance of the coil is measured directly instead of the change of the impedance. They are the simplest and most commonly used transducers. However a disadvantage in using absolute transducers is that small changes of the impedance due to a flaw are often superimposed on the large value. Also, factors such as lift – off and probe wobble can mask the small changes of coil impedance due to defects and make the interpretation of the signal rather difficult.

Differential eddy current transducers often consist of a pair of coils that are connected in opposition so that the net value of the impedance is cancelled out when both coils are in identical situations. Therefore, only difference between impedance of the two coils is picked up. The influence of other factors such as lift – off and probe wobble is eliminated because they generally have the same impact on both coils. Differential eddy current transducers have higher sensitivity to changes of impedance due to presence of flaw than absolute eddy current transducers do.

Eddy current array eddy current transducers consist of an array of either absolute transducers or differential transducers. One application of using array transducers is in aircraft engine disk inspection. Each disk contains 30 slots. An array transducers consisting of eight differential transducers is used to scan the surface of each slot resulting in a total of 16 signals (real and imaginary parts of the complex impedance) are obtained for each slot. These signals are processed using specific signal and image processing techniques to indicate the presence of the defect.

2.5 EC Inspection of Steam Generator Tubes in Nuclear Power Plants

Eddy current testing methods are widely used for inspecting heat – exchange tubes in steam generators in nuclear power plants. Steam generators are used to transfer thermal energy from the primary side to the secondary side. Figure 2.7 shows the layout of the heat transfer system in nuclear power plants. Heat generated by the nuclear reactor is transferred to the primary coolant that circulates inside the nuclear vessel. The primary coolant is circulated through a set of tubes in steam generator where the heat is

transferred to a mixture of steam and water through tube walls. The steam is circulated inside the secondary loop and is used to drive the steam turbines that are used to generate electricity. While in primary loop, the coolant is radioactive, the coolant in the secondary loop is not radioactive. It is critical to keep the radioactive coolant from contaminating the nonradioactive coolant water. This means that the steam generator tubes have to be inspected frequently in order to keep the whole system safe because any potential leak in those tubes can result in disastrous consequences.

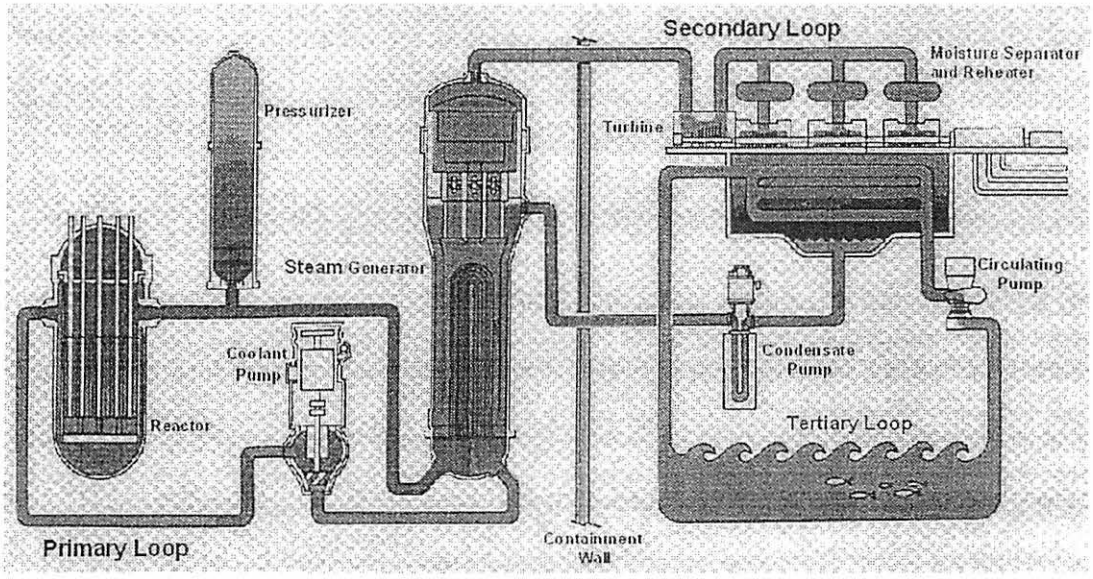

Figure 2.7 Heat transfer system in nuclear power plants [42]

The inspection process involves inserting an eddy current probe into one end of the heat exchange tube and moving it until it reaches the other end. The probe is then pulled out at a constant speed and the impedance of the probe is measured as a function of time (or location in the tube). The data obtained in the inspection process must be calibrated to compensate for variations due to the variation in probe characteristics and instrument

setting. The calibration tube has the same dimension and material properties as the tubes to be inspected. Artificial defects are machined in the calibration tube to provide a reference for later data analysis.

Four excitation frequencies are used in each inspection, and the data obtained for each frequency can be in both absolute and differential mode.

Bobbin coil eddy current probe, widely used in the inspection of steam generator tubes, produces a one – dimensional signal. Although bobbin coil is very good at detecting axial defects, it is not very sensitive to circumferential defects. Therefore, alternate types of probe, such as the rotating pancake coil (RPC) probe, is used in recent years. When inspecting the tubes, the probe is rotating with a constant speed as well as moving along the tube axially. It has the obvious advantage that it is equally sensitive to both axial and circumferential defects. Also, the data obtained using rotating probe can be viewed as an image for each tube instead of a one – dimensional data in the case of bobbin coil inspection. This data can give the operator better view of the situation for each tube. The eddy current data processed in this thesis is obtained using the rotating probe.

2.6 Defect Characterization Problem

The crucial problem in tube inspection is defect characterization. This involves estimation of the characteristics of the defect, such as the shape, orientation, width, length, and depth of the defect.

Defect characterization problem is often very difficult to solve due to the lack of information about the inspection system, the tube under inspection, and noise generated during the inspection process. Artifacts are also introduced in the data by the finite size of the probe. A commonly used approach for addressing this problem is to assume that the measured signal is a convolution of the defect footprint and the probe response. Deconvolution methods can then be used to remove the effect of the probe and give an estimate of the true defect footprint. Most deconvolution algorithms require a priori knowledge of the kernel function. This knowledge is crucial for improving the performance of the algorithm, but in general it is very difficult to obtain. Consequently, blind deconvolution method that does not require the knowledge of kernel function is more suitable to address defect characterization problem.

In this thesis, an iterative blind deconvolution algorithm based on Richardson – Lucy algorithm is described for removing the effect of the probe point spread function.

CHAPTER 3. BLIND DECONVOLUTION TECHNIQUES

3.1 Introduction

In many applications including astronomy, medical imaging, and remote sensing [3, 14, 15], images are often degraded by blur and additive noise. Very often this degradation is represented by the following linear model:

$$\begin{aligned} g(x,y) &= f(x,y) * h(x,y) + n(x,y) \\ &= \sum_{n,m} f(n,m)h(x-n,y-m) + n(x,y) \end{aligned} \tag{2.1}$$

where $g(x,y)$, $f(x,y)$, and $h(x,y)$ denote respectively the degraded 2 – dimensional image , the original image and the linear shift-invariant blur which is generally referred to as the point spread function(PSF); * denotes the 2 – D convolution operation, $n(x,y)$ is the additive noise, and x, y, n, m $\in$ Z, the set of all integers.

Image restoration technique are used to reconstruct the original image $f(x,y)$ from the degraded observation, $g(x,y)$, with or without the presence of additive noise, $n(x,y)$. Since the degraded image, $g(x,y)$, is assumed to be the convolution of original image, $f(x,y)$, and the PSF, $h(x,y)$, it is quite obvious that deconvolution techniques perform a very important role in image restoration. If the PSF, $h(x,y)$, is assumed to be known explicity, we have a classical linear image restoration problem. A variety of techniques have been developed to deal with the classical linear image restoration problems, such as inverse filtering, Wiener filtering, least – squares filtering, recursive Kalman filtering, and constrained iterative deconvolution [16, 17, 18, 19].

Unfortunately, in most practical applications, it is often difficult, if not impossible, to obtain the information about the original image a pirori, and it is also very difficult to accurately model the PSF. This results in limiting the applications of classical image restoration techniques. In these applications, the original image, $f(x,y)$, has to be estimated directly from the degraded image, $g(x,y)$, with partial or no information about the PSF, $h(x,y)$, and the original image, $f(x,y)$. Such an estimation problem is often called *blind deconvolution.*

For the past two decades, blind deconvolution has been an active research area due to its obvious advantage over classical image restoration methods. A variety of techniques which combine the PSF identification and image restoration have been developed and implemented in the areas of medical imaging, remote sensing, and astronomy and so on. In the rest of this chapter, some of the important properties of blind deconvolution are described and some commonly used blind deconvolution techniques are discussed.

3.2 Properties of Blind Deconvolution

As described earlier, degradation due to blurring process can be modeled in the form of equation (3.1). Figure 3.1 gives a general overview of linear degradation model [14]. The additive noise, $n(x,y)$, may include electronic noise, photoelectric noise, film noise, or quantization noise, depending on the applications.

The general blind convolution problem involves estimation of the original image, $f(x,y)$, from the degraded image, $g(x,y)$, with partial or no information of the original

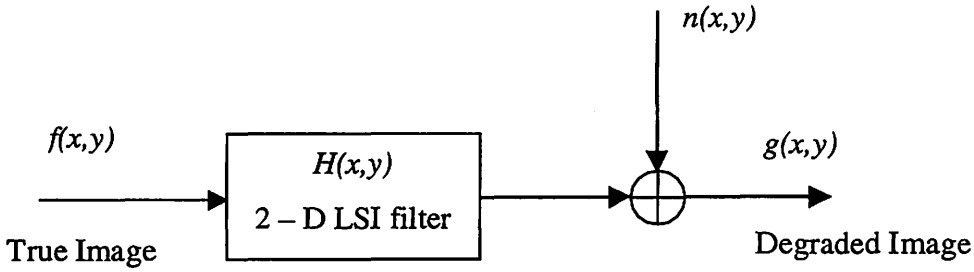

Figure 3.1 A general linear degradation model

image, $f(x,y)$, the PSF, $h(x,y)$, or the additive noise, $n(x,y)$. Figure 3.2 gives the general model of a blind deconvolution approach [14].

Some important characteristics of the blind deconvolution problems include:

1. The original image and PSF must be *irreducible* for uniqueness. An irreducible signal is a signal that can not be exactly expressed as the convolution of two or more component signals, under the assumption that the two – dimensional delta function is not a component signal [14]. This is very important if a unique solution is expected to be obtained. For example, if the original image $f(x,y)$ is reducible, e.t., $f(x,y)=f_1(x,y)*f_2(x,y)$, then

$$g(x,y) = f_1(x,y) * f_2(x,y) * h(x,y) \tag{3.2}$$

Since the degraded image $g(x,y)$ consists of three components, it is impossible to decide which component(s) belong to the original image and the PSF.

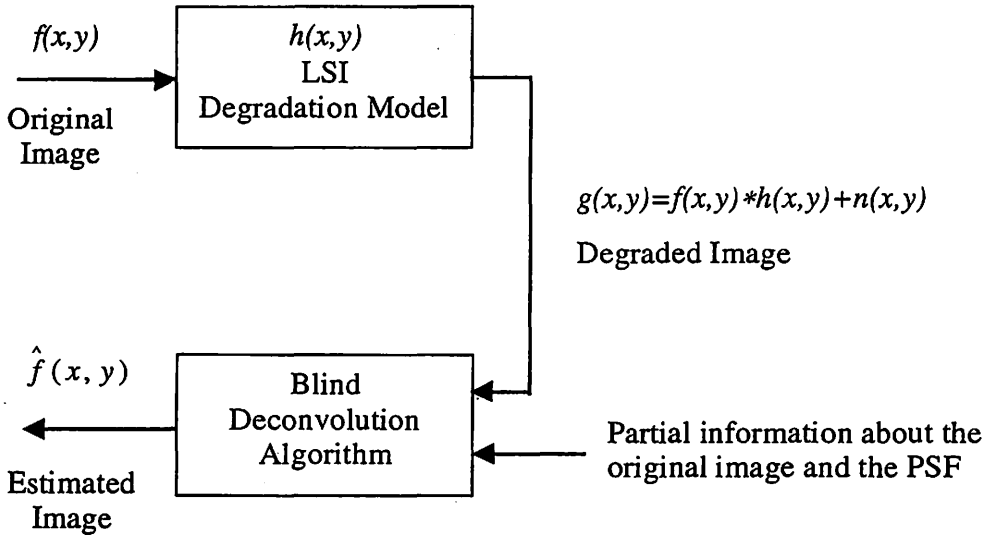

Figure 3.2 A general blind deconvolution system model

2. In classical image restoration, the objective is to obtain an estimate of the original image that is as close to the true image as possible. In blind deconvolution problem, the result maybe a scaled and shifted version of the original image [21]. That is:

$$\hat{f}(x,y) = Kf(x-a, y-b) \tag{3.3}$$

where $\hat{f}(x,y)$ is an estimate of the original image obtained by using a blind deconvolution technique, and K, a, and b are arbitrary real constant and denote the scaling factor, the displacement in x – axis, and the displacement in y – axis respectively. It is usually impossible to find out the value of K, a, and b after blind deconvolution without adding additional constrains.

3. Generally, blind deconvolution problem is an ill – conditioned problem. This implies that in practical applications, a small change in the degraded image can produce large changes in the obtained results. This introduces difficulties of stability and robustness.
4. Due to the presence of additive noise, it is impossible to obtain a solution that is exactly the same as the true image. The reason is that the only information available about the noise is its statistical information. Therefore, noise cannot be removed by simply subtracting $n(x,y)$ from the degraded image $g(x,y)$. In some cases, it gets even worse when the additive noise makes $g(x,y)$ irreducible. Hence blind deconvolution provides only an approximate solution.
5. Since only partial information of the degradation system is available, the algorithm can converge to local minima and hence not be unique. With change of initialization conditions and addition of other constrains, the deconvolution process may converge to different optimal solutions [22].

Due to the numerous applications of blind deconvolution, a lot of research has been done to develop fast and robust blind deconvolution algorithms. In the next section, typical blind deconvolution techniques are reviewed.

3.3 Typical Blind Deconvolution Techniques

Generally, blind deconvolution techniques can be divided into two categories. The first category includes the techniques that estimate the PSF before estimating the original image. The major advantage of these methods is low computational complexity. The

disadvantage is that they can be used only in the case that the PSF is known to have special characteristics [14]. A simple example of this claim is the blur identification problem. Most blind deconvolution techniques belong to the second category, which estimates the original image and the PSF simultaneously. While it is computationally more complex, it has a wider range of applications. This category can be further divided into two classes: namely parametric and nonparametric. The parametric approaches assume that the model of the original image or the PSF is known, and the nonparametric approaches utilize deterministic constraints on the original image such as nonnegativity and known finite support.

3.3.1 Zero Sheet Separation

Zero sheet separation was first introduced by Lane and Bates [21] in 1987. It is a technique that belongs to the second category of approaches. Although it is not commonly used, it is worth reviewing since it gives valuable insight into the blind deconvolution problem.

The theory of zero sheet separation method is based on the analytical properties of the Z – Transform in multiple dimensions: the zeros of the Z – Transform of a K – dimensional signal is almost always continuous and lies on a ($2K$-2) – dimensional hypersurface [23].

Several basic assumptions are made on the degradation model [21] such as:

1. No additive noise is present in the degradation system, that is

$$g(x,y) = f(x,y) * h(x,y) \tag{3.4}$$

2. Both the original image *f(x,y)* and the PSF *h(x,y)* have finite support.

3. *f(x,y)* and *h(x,y)* are irreducible.

Based on the assumption (1), the following equation holds:

$$G(z_1, z_2) = F(z_1, z_2)H(z_1, z_2) \tag{3.5}$$

where $G(z_1, z_2)$, $F(z_1, z_2)$, and $H(z_1, z_2)$ are the Z – Transform of *g(x,y)*, *f(x,y)*, and *h(x,y)* respectively. This equation indicates that 2 – D blind deconvolution problem is equivalent to factoring the 2 – D polynomial $G(z_1, z_2)$. More details can be found in [24].

Zero sheet separation method has a major disadvantage. Since it does not take the additive noise into account, it is very sensitive to noise. And this leads to the limitation of its implementation in real applications.

3.3.2 A Priori Blur Identification Method

A priori blur identification method belongs to the first category mentioned in section 3.2, where the PSF is estimated first. In order to successfully estimate the PSF, some assumptions have to be made. These assumptions include the characteristics of the PSF and availability of a known parametric form of the PSF. Based on the assumptions of PSF and knowledge of the original image and the degraded image, it is possible to completely

identify the PSF. Once the PSF is obtained, one of the classical image restoration techniques can be used to estimate the original image.

There are two commonly used PSF forms [25]. One is horizontal camera motion blur of length 2d that has the form:

$$h(x,y)=\begin{cases}0 & y\neq 0,-\infty\leq x\leq\infty\\ \dfrac{1}{2d} & y=0,-d\leq x\leq d\end{cases}. \tag{3.6}$$

The frequency domain zeros of this type of PSF are located on the lines perpendicular to the direction of the blur and with equal interval of *1/d*. The other commonly used PSF is that of a defocused lens system with a circular aperture that has the form:

$$h(x,y)=\begin{cases}0 & \sqrt{x^2+y^2}>r\\ \dfrac{1}{\pi r^2} & \sqrt{x^2+y^2}\leq r\end{cases} \tag{3.7}$$

The frequency domain zeros of this type of are located on the concentric circles around the origin that are periodic in *r*.

To achieve successful restoration, it is important to estimate the PSF as accurately as possible. One approach for completely identifying the PSF is by using the properties of frequency domain zeros described in the last section. If the additive noise is ignored, the degradation model shown in equation (3.1) is simplified to equation (3.4). This leads to the frequency domain relation:

$$G(u,v)=F(u,v)H(u,v)\quad u,v\in\Re \tag{3.8}$$

Therefore, the problem of identifying the PSF is equivalent to the problem of deermining the zeros of $F(u,v)$ and $H(u,v)$. Once the zeros of $H(u,v)$ has been identified, the parameters of the PSF can be decided according to the properties of frequency domain zeros.

The blur identification method based on the frequency domain zeros is one of the most popular and successful methods used due to its computational simplicity and reliability. But it also has a major drawback of not being robust in the presence of the additive noise because the additive noise may change the distribution of the frequency domain zeros.

3.3.3 ARMA Parametric Estimation Methods

In the blur identification method, the PSF is assumed to have certain form with one or two parameters. The assumption in general is not true in most practical applications. Another commonly used parametric method is the ARMA estimation method.

ARMA estimation method is based on the concept that the degraded image can be modeled as an autoregressive moving average (ARMA) process. The identification of ARMA coefficients leads to the estimation of the original image and the PSF.

The ARMA model of the degraded image involves the following two parts.

1. The original image *f(x,y)* is modeled as a 2 – D autoregressive (AR) process described by the following equation:

$$f(x,y) = \sum_{\substack{(l,m)\in R_a \\ (l,m)\neq(0,0)}} a(l.m) f(x-l, y-m) + v(x,y) \qquad (3.9)$$

where the parameters *a(l,m)* are the AR coefficients with *a(0,0)* being 1, and *f(x,y)* is the original image. The term *v(x,y)* is the modeling error that is a zero-mean homogeneous noise process independent of *f(x,y)*, and R_a is the support of the AR coefficients *a(l,m)*. The AR coefficients *a(l,m)* are chosen to minimize the variance of modeling error *v(x,y)*.

2. In most practical applications, the PSF has finite support and it can be modeled as a 2 – D moving average (MA) process shown as:

$$g(x,y) = \sum_{(l,m)\in R_h} h(l,m) f(x-l, y-m) + n(x,y) \tag{3.10}$$

where the parameter *h(l,m)* is the PSF or the MA coefficient, *n(x,y)* is the additive noise that is a zero – mean Gaussian process, and R_h is the support of the PSF *h(l,m)*.

Equation (3.9) and (3.10) can be lexicographically ordered to form compact matrix – vector equations:

$$f = Af + v \tag{3.11}$$

and

$$g = Hf + n \tag{3.12}$$

Lexicographic ordering is used to map an $M \times N$ matrix to a column vector. This row – ordered vector is defined as:

$$X^T = [x(1,1)\, x(1,2) \cdots x(1,N) \cdots\cdots x(M,1)\, x(M,2) \cdots x(M,N)]^T \tag{3.13}$$

where $x(l,m)$ is the (l,m)th element of the $M \times N$ matrix [26].

Combining equation (3.11) and (3.12), the ARMA model can be expressed as

$$g = H(I - A)^{-1} v + n \tag{3.14}$$

where I is the identity matrix.

It is very difficult to identify the ARMA coefficients $a(l,m)$ and $h(l.m)$ because of computationally complexity. To get around this difficulty, several assumption are made [14]:

1. The PSF is positive, and the restoration process is a conservative process, i.e.,

$$\sum_{(l.m)\in R_h} h(l,m) = 1 \tag{3.15}$$

2. The PSF is symmetric.

3. The PSF has a known parametric form with a few unknown parameters.

Under these assumptions, different methods can be used to identify the ARMA coefficients. Such as the Maximum – Likelihood (ML) approach [28], and General Cross – Validation (GCV) approach [29]. In ML approach, estimation the coefficients is made so that the probability or likelihood of obtaining an accurate estimate of the original image given the coefficient set, $\{\{a(l,m)\}, \{h(l,m)\}, \sigma_n^2, \sigma_v^2\}$, is maximized. σ_n^2 and σ_v^2 are the variances of $n(x,y)$ and $v(x,y)$ respectively. A variety of methods, such as gradient – based method, expectation – maximization (EM) method, and least squares method, are used to solve the maximization problem [27]. In GCV approach, data is divided into two sets: an estimation set and a validation set. The estimation set is used to obtain a model or

estimate based on a particular parameter value. The validation set is used to validate the performance of model. Both data sets are used for both purposes.

One major advantage of ARMA parametric estimation method is that it takes the additive noise into account when developing the model. Therefore, it is less sensitive to the noise. A drawback of this method is that it can converge to local minima. Another drawback is that it imposes constraints on the PSF when developing the model, and this may limit the application of this method.

3.3.4 Nonparametric Estimation Methods

Unlike other blind deconvolution techniques just introduced, nonparametric estimation methods do not assume any parametric models of the original image or the PSF. Instead, they utilize some deterministic constraints of the original image for estimating the PSF and the original image. Some of these constraints include nonnegativity, known finite support, and existence of invariant edges. Methods in this class include simulated annealing (SA) method [30], nonnegativity and support constraints recursive inverse filtering (NAS – RIF) [31, 32], and iterative blind deconvolution (IBD) method [33, 34, 35, 36]. All three methods are described in the rest of this section.

3.3.4.1 Iterative Blind Deconvolution Method

Besides the constraints stated above, the IBD method also imposes the nonnegativity and known finite support constraint to the PSF. In IBD method, the PSF and the original

image are estimated sequentially in each iteration. The blind deconvolution process terminates when convergence criterion is met. Detailed information about IBD method will be presented in next chapter.

The reasons for the wide usage of IBD method include its low computational complexity and its robustness in the presence of additive noise. The major disadvantage of IBD method is that it sometimes does not converge to the optimal solution. Additionally, the restoration is sensitive to the initial estimates of the original image and the PSF.

3.3.4.2 Simulated Annealing Method

Simulated annealing (SA) method is another nonparametric blind deconvolution method. The reason it is called simulated annealing is that it is analogous to the annealing of metals. It imposes the same deterministic constraints as the IBD method does, and changes the blind deconvolution problem to the problem of the minimization of the following cost function [37]:

$$J(\hat{f}(x,y),\hat{h}(x,y)) = \sum_{\forall(x,y)}[\hat{f}(x,y) * \hat{h}(x,y) - g(x,y)]^2 \qquad (3.18)$$

where $\hat{f}(x,y)$, $\hat{h}(x,y)$, and $g(x,y)$ are the estimation of original image, PSF, and the degraded image respectively.

Using the deterministic constraints, J is minimized iteratively with respect to $\hat{f}(x,y)$ and $\hat{h}(x,y)$. In each iteration, the parameters are perturbed randomly. The perturbation is accepted if J is decreased. If J is increased, the perturbation is accepted

with a probability of $p = exp(-\Delta J/T_k)$, where ΔJ is the change of the value of J, and T_k is called the temperature parameter that is used to control the speed of convergence. As the process continues, the value of T_k slowly reduced analogous to the annealing of metals.

SA method is very reliable and produces reasonable results in the presence of additive noise. But the slow convergence and high computational complexity level are major obstacles limiting its use in practical application. Also, during the restoration process, T_k has to be reduced slowly. Otherwise, the method may converge to local minima instead of global minima.

3.3.4.3 NAS – RIF Method

The nonnegativity and support constraints recursive inverse filtering (NAS – RIF) method is another commonly used nonparametric estimation method. While it imposes constraints on the original image similar to the IBD and SA methods, the only assumptions made on the PSF is that it is absolutely summable, that is $\sum_{\forall(x,y)} |h(x,y)| < \infty$, and that it has an inverse $h^{-1}(x,y)$ that is also absolutely summable. The approach can be used when the exact support of PSF is unknown.

Figure 3.3 shows a general NAS – RIF deconvolution system model. $u(x,y)$ is a variable FIR filter which takes the degraded image $g(x,y)$ as input. *NL* denotes the nonlinear filter that imposes the deterministic constraints on the estimated original image $\hat{f}(x,y)$. Either nonnegativity or the known finite support or both can be applied to $\hat{f}(x,y)$. When both constraints are used, the following cost function is obtained [31]:

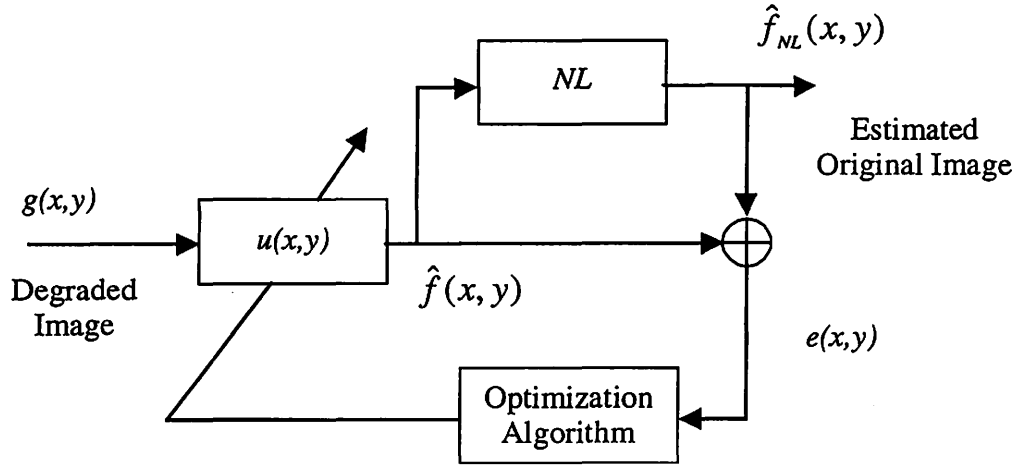

Figure 3.3 A general NAS – RIF system model [14]

$$J(u)=\sum_{(x,y)\in D_{sup}}\hat{f}^2(x,y)\left[\frac{1-\mathrm{sgn}(\hat{f}(x,y))}{2}\right] + \sum_{(x,y)\in \overline{D}_{sup}}\left[\hat{f}(x,y)-L_B\right]^2+\gamma\left[\sum_{\forall(x,y)}u(x,y)-1\right]^2 \tag{3.19}$$

where $\hat{f}(x,y)=g(x,y)*u(x,y)$, D_{sup} is the set of all pixels inside the support region of $f(x,y)$, and $\overline{D}_{sup}$ is the set of all pixels outside the support region. L_B is the pixel value of the background of $f(x,y)$, the variable γ is nonzero only when L_B is zero, i.e., the background color is black. A variety of methods including steepest – descent and conjugate gradient minimization can be used to minimize $J(u)$ and obtain the deconvolved image $\hat{f}(x,y)$.

The NAS – RIF method does not require the knowledge of the finite support of the PSF, and has better convergence property than IBD method. Compared with SA method,

NAS – RIF method has lower computational complexity level. However it is sensitive to the presence of additive noise.

Other nonparametric estimation methods using higher order statistical information of the original image to minimize a cost function can be found in [38, 39, 40].

CHAPTER 4. DEFECT CHARACTERIZATION USING BLIND DECONVOLUTION

4.1 Problem Statement

Eddy current testing techniques are widely used to inspect steam generator tubes in nuclear power plants. Different kinds of probes, such as bobbin probes and rotating probes, are used in these inspections. The data obtained using EC techniques are analyzed using a variety of signal and image processing methods and useful information is extracted. This information can be used to indicate the presence of the defect on the inner and outer surface of the tubes. The data can also be further analyzed to estimate the shape, width, length, and depth of the defects. This problem is called defect characterization.

Defect characterization in general is fraught with difficulties due to several reasons. One major reason is the lack of knowledge of the inspection system and tube under inspection. Another reason is that the probe speed changes during the inspection process. This may introduce errors in the collected data. Additive noise generated during the scan due to presence of dirt and surface roughness can also present problems. Besides these, when an analog signal is sampled to generate a digital signal, quantization errors are introduced. This can lead to the additional distortion of the signal. All these reasons make defect characterization in steam generator tubes a very challenging task.

The approach proposed in this thesis for data processing consists of 3 steps: 1) De-noising; 2) Deconvolution; 3) Defect Characterization. In the first step the signal is

filtered using conventional procedures to eliminate the additive noise associated with the measurement system. The second step is used to eliminate the "smearing" of the true signal due to finite size or point spread function (PSF) of the sensor coil. In the third step, the processed and deconvolved data is used in a defect characterization algorithm for estimating the defect profile. This thesis is focused on addressing the deconvolution problem in the second step.

4.2 Deconvolution of Eddy Current Signal

A commonly used approach for eliminating the "smearing" effect of the probe is to assume that the observed signal is a convolution of the true defect profile and the probe PSF. One can then use deconvolution methods to extract the true defect image from the knowledge of measured data and probe PSF. Since the knowledge of the inspection system and the tube and probe PSF are generally unknown, blind deconvolution, discussed in the chapter 3, is shown to be more suitable to handle this problem.

Equation (3.1) gives a general degradation model that can also be used to represent the defect characterization problem. Neglecting the presence of the additive noise, the equation can be simplified as follows:

$$\begin{aligned} g(x,y) &= f(x,y) * h(x,y) \\ &= \sum_{n,m} f(n,m)h(x-n,y-m) \end{aligned} \tag{4.1}$$

where $g(x,y)$, $f(x,y)$, and $h(x,y)$ are the observed or raw signal, true defect footprint, and probe point spread function (PSF) respectively. Under this assumption, the

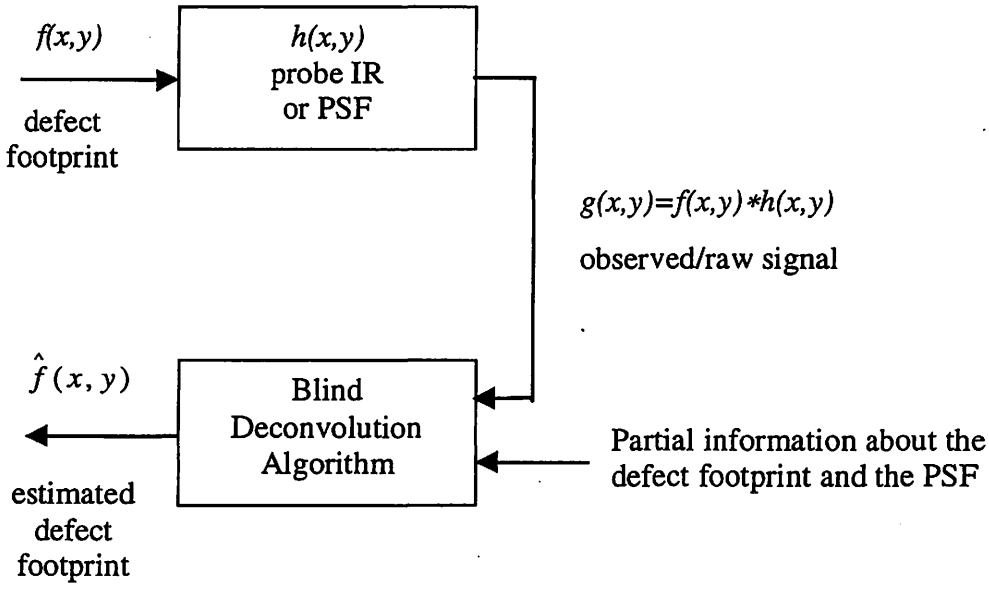

Figure 4.1 Schematic of Blind Deconvolution Method

blind deconvolution problem can be modeled as shown in figure 4.1. The partial information of the true defect footprint and PSF includes nonnegativity and finite support region.

In a practical situation as in steam generator tube inspection in nuclear power plants, one of the concerns of defect characterization problem is the computational complexity due to the large amount of tubes to be inspected in a short period of time. Among all the blind deconvolution methods, iterative blind deconvolution (IBD) method has an advantage over other methods in terms of computational complexity. Consequently this thesis focuses on the iterative blind deconvolution method for obtaining both the probe PSF and estimate of the defect footprint. Both the probe response and the defect footprint are estimated sequentially in each iteration according to the observed data and other

known a priori information of the true defect footprint and probe response. No assumption is made about the shape of the probe response or the defect footprint when performing blind deconvolution. Instead, known deterministic constraints are imposed such as nonnegativity and finite support of the defect profile and the probe response. The deconvolution procedure is terminated when the result converges. Figure 4.2 shows a general iterative blind deconvolution model. (In the figure, k represents the number of iteration.

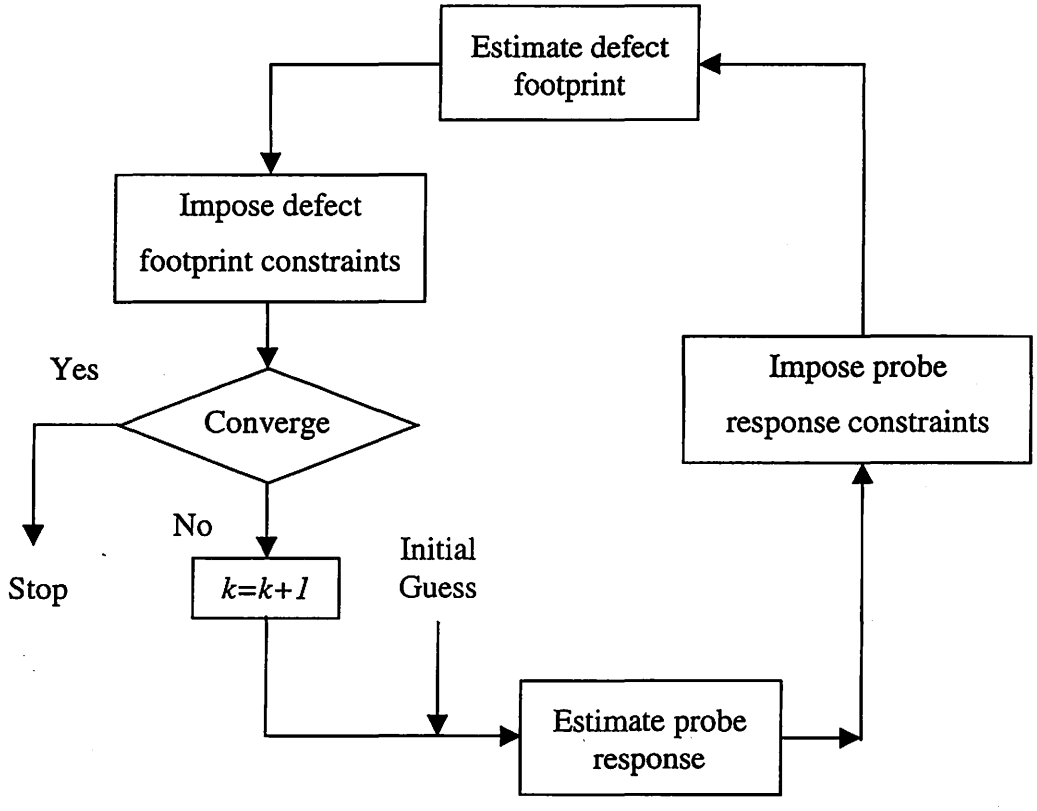

Figure 4.2 A general iterative blind deconvolution model

4.3 Iterative Blind Deconvolution Using Wiener Filter

A number of algorithms can be included in the category of iterative blind deconvolution. Popular algorithms is the iterative Wiener filtering. It is based on the classical 2 – dimensional Wiener filter that is widely used in image restoration and other image processing applications. In iterative Wiener filter method, $\hat{f}(x,y)$, $\hat{h}(x,y)$, and $g(x,y)$ denote the estimate of defect footprint, probe impulse response, and the observed signal respectively, and at *k*th iteration, the updated $\hat{f}_k(x,y)$ and $\hat{h}_k(x,y)$ are obtained through the following two equations [33, 34]:

$$\hat{H}_k(u,v) = \frac{G(u,v)\hat{F}_{k-1}^{*}(u,v)}{\left|\hat{F}_{k-1}(u,v)\right|^2 + \alpha \Big/ \left|\hat{H}_{k-1}(u,v)\right|^2} \tag{4.2}$$

and

$$\hat{F}_k(u,,v) = \frac{G(u,v)\hat{H}_k^{*}(u,v)}{\left|\hat{H}_k(u,v)\right|^2 + \alpha \Big/ \left|\hat{F}_{k-1}(u,v)\right|^2} \tag{4.3}$$

where $G(u,v)$, $\hat{H}_k(u,v)$, and $\hat{F}_k(u,v)$ are the Fourier transforms of $g(x,y)$, $\hat{h}_k(x,y)$, and $\hat{f}_k(x,y)$ respectively and $(\cdot)^*$ represents the complex conjugate of $(\cdot)$. α is a real constant representing the energy of the additive noise which is determined before the deconvolution process using a priori knowledge of the noise level. In the case of

unknown noise level, a value of 0.1 is often chosen for α. In each iteration, deterministic constraints are applied to the estimated defect footprint and the probe impulse response. A general iterative Wiener filter model is shown in figure 4.3.

One advantage of iterative Wiener filter is its low computational complexity. Further, since it is based on classical 2 – dimensional Wiener filter, it shows a certain level of robustness in the presence of additive noise.

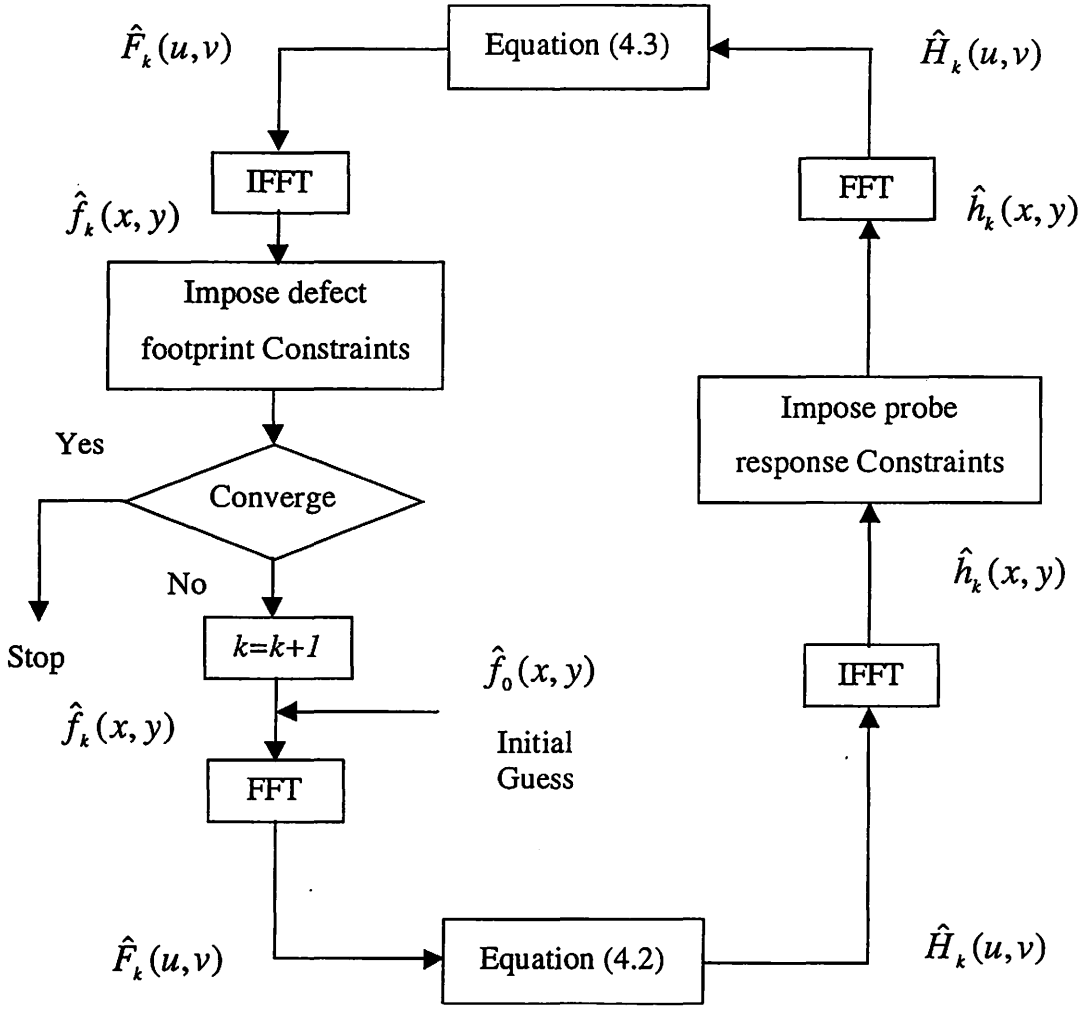

Figure 4.3 A general iterative Wiener filter system model

4.4 Richardson – Lucy Algorithm

Another common iterative blind deconvolution method is based on the Richardson – Lucy algorithm developed by Richardson [5] and Lucy [6] in 1970s. It was originally used in the area of statistical astronomy for estimating the true image from the blurred observed image. The fundamental idea in Richardson – Lucy algorithm is to model the true image, point spread function, and observed image as probability – frequency functions and iteratively estimate the true image and point spread function by applying Bayes's theorem. The problem in this case is to estimate the frequency distribution function $\psi(\xi')$ of ξ' from known observations $x_1', x_2', \cdots, x_N'$ which are discrete samples of a continuous function defined by the following distribution function:

$$\phi(x) = \int \psi(\xi) P(x|\xi) d\xi \tag{4.4}$$

where $P(x|\xi)d\xi$ is the conditional probability that x' is in the interval $(x, x+dx)$ when ξ' is equal to ξ. If the conditional probability function $P(x|\xi)$ is considered as the point spread function or the kernel, the integral equation (4.4) is nothing but a one – dimensional continuous version of degradation model described by equation (4.1). This similarity between these two models is exploited in the statistical method for solving the image degradation problem.

Generally, the information about probability distribution function $\psi(\xi)$ is hard to obtain, except for the following commonly used assumptions:

$$\int \psi(\xi) d\xi = 1 \tag{4.5}$$

and

$$\psi(\xi) \geq 0 \tag{4.6}$$

Although it is very straightforward to use a numerical method to calculate the integral equation (4.4), it often results in poor solutions unless the sample size N is large. In order to overcome this problem, an iterative method was developed.

Assume that $Q(\xi|x)dx$ is the conditional probability that ξ is in the interval $(\xi, \xi + d\xi)$ when x' is equal to x. Under this assumption, the probability that $x' \in (x, x + dx)$ and $\xi' \in (\xi, \xi + d\xi)$ is:

$$\phi(x)dx \times Q(\xi|x)d\xi \tag{4.7}$$

On the other hand, the above probability is equal to:

$$\psi(\xi)d\xi \times P(x|\xi)dx \tag{4.8}$$

Hence, we have:

$$\phi(x) = \frac{\psi(\xi) \times P(x|\xi)}{Q(\xi|x)} \tag{4.9}$$

Substituting equation (4.9) into equation (4.4), we have:

$$Q(\xi \mid x) = \frac{\psi(\xi) \times P(x|\xi)}{\int \psi(\xi) \times P(x|\xi)d\xi} \tag{4.10}$$

which is essentially Bayes's theorem of conditional probability.

Also, the following equation is generally true:

$$\psi(\xi) = \int \phi(x) Q(\xi|x) dx \tag{4.11}$$

which is just the inverse integral equation of equation (4.4). Although this integral equation cannot be used directly to calculate $\psi(\xi)$ because the conditional probability $Q(\xi|x)$ is generally unknown, it gives us a possible iterative method to estimate $\psi(\xi)$. That is, given an initial guess of $\psi(\xi)$ and known conditional probability function $P(x|\xi)$, equation (4.10) can be used to estimate the conditional probability function $Q(\xi|x)$. This estimate is then integrated over $\tilde{\phi}(x)$, which is an approximation to $\phi(x)$ obtained from the observed data., according to equation (4.11) to get an updated estimate of $\psi(\xi)$. This process is repeated until a reasonable solution is achieved. In other words, if $\psi^r(\xi)$ is the estimate in *r*th iteration, the estimate in (*r*+1)th iteration, $\psi^{r+1}(\xi)$, is

$$\psi^{r+1}(\xi) = \int \tilde{\phi}(x) Q^r(\xi|x) dx \tag{4.12}$$

where

$$Q^r(\xi \mid x) = \frac{\psi^r(\xi) P(x|\xi)}{\phi^r(x)} \tag{4.13}$$

and

$$\phi^r(x) = \int \psi^r(\xi) P(x|\xi) d\xi \tag{4.14}$$

Substituting equation (4.13) into equation (4.12) and eliminating $Q^r(\xi|x)$ from equation (4.12), we have:

$$\psi^{r+1}(\xi) = \psi^r(\xi) \int \frac{\tilde{\phi}(x)}{\phi^r(x)} P(x|\xi) d\xi \tag{4.15}$$

Equation (4.15) shows that the constraint condition stated in equation (4.6) is conserved, i.e. $\psi^{r+1}(\xi) \geq 0$ if $\psi^0(\xi) \geq 0$. It also shows that the iterative algorithm converges when $\tilde{\phi}(x) = \phi^r(x)$.

Equation (4.14) and (4.15) together constitute the iterative technique in the one – dimensional case. The extension to the 2 – dimensional case is straightforward. In the 2 – dimensional case, the iterative technique is based on the following equations:

$$\psi^{r+1}(\xi,\eta) = \psi^r(\xi,\eta) \iint \frac{\tilde{\phi}(x,y)}{\phi^r(x,y)} P((x,y)|(\xi,\eta)) d\xi d\eta \tag{4.16}$$

where

$$\phi^r(x,y) = \iint \psi^r(\xi,\eta) P((x,y)|(\xi,\eta)) d\xi d\eta \tag{4.17}$$

The 2 – dimensional iterative technique can be easily implemented on image data in classical image restoration applications under the assumption that the conditional probability function $P((x,y)|(\xi.\eta))$ is equal to the normalized point spread function or the kernel centered at the point (ξ,η), i.e. $H(x-\xi, y-\eta)$:

$$\psi^{r+1}(\xi,\eta)=\psi^{r}(\xi,\eta)\iint\frac{\tilde{\phi}(x,y)}{\phi^{r}(x,y)}H(x-\xi,y-\eta)dxdy \tag{4.16}$$

where

$$\phi^{r}(x,y)=\iint\psi^{r}(\xi,\eta)H(x-\xi,y-\eta)d\xi d\eta \tag{4.17}$$

In this case, the initial guess $\psi^{0}(\xi,\eta)$ is a nonnegative function and has the same integrated intensity as the observed image.

4.5 Blind Deconvolution Using Richardson – Lucy Algorithm

Equation (4.16) and (4.17) gives us a possible method to solve the classical image restoration problem under the assumption that $\psi(\xi,\eta)$, $\phi(x,y)$, and $H(x-\xi,y-\eta)$ are the true image $f(x,y)$, the observed degraded image $g(x,y)$, and the point spread function $h(x,y)$ in the image degradation system. Another assumption is that the point spread function is known a priori. Equations (4.16) and (4.17) can be combined and expressed in the compact form:

$$f^{r+1}(x,y)=\left\{\left[\frac{g(x,y)}{f^{r}(x,y)\otimes h(x,y)}\right]\otimes h(-x,-y)\right\}f^{r}(x,y) \tag{4.18}$$

where $\otimes$ denotes the 2 – dimensional convolution operation.

In practice, the point spread function has a complex form and is not known in advance. In Richardson – Lucy algorithm, an iterative equation for estimating the updated point spread function is needed. In fact, the derivation of this equation is quite

straightforward. It can be easily obtained by exchanging the role of $h(x,y)$ and $f(x,y)$. In this case, the following two equations present the fundamental ideas of blind deconvolution using the Richardson – Lucy algorithm [4.3, 4.4]:

Estimate the PSF iteratively according to

$$h^{r+1}(x,y)=\left\{\left[\frac{g(x,y)}{h^r(x,y)\otimes f^r(x,y)}\right]\otimes f^r(-x,-y)\right\}h^r(x,y) \tag{4.19}$$

and estimate the true image according to

$$f^{r+1}(x,y)=\left\{\left[\frac{g(x,y)}{f^r(x,y)\otimes h^{r+1}(x,y)}\right]\otimes h^{r+1}(-x,-y)\right\}f^r(x,y) \tag{4.20}$$

In early 1990s, Holmes first implemented the Richardson – Lucy algorithm in blind deconvolution applications [41]. In his method, each iteration is divided into two steps: the first step is to estimate the updated point spread function $h^{r+1}(x,y)$ given the knowledge of observed degraded image $g(x,y)$, estimate of the point spread function $h^r(x,y)$, and estimate of the true image $f^r(x,y)$ according to equation (4.19), and in the second step the updated true image $f^{r+1}(x,y)$ is estimated given the knowledge of observed degraded image $g(x,y)$, estimate of the point spread function $h^{r+1}(x,y)$ and estimate of the true image $f^r(x,y)$ according to equation (4.20). Also worth noting is that the initial guess of true image $f^0(x,y)$ and point spread function $h^0(x,y)$ are

needed and these initial guess must satisfy the nonnegativity constraints described in equation (4.6).

The following figures show the performance of blind deconvolution method using both iterative Wiener filter and Richardson – Lucy algorithm. The degraded image is generated from a synthetic image (figure 4.4(a)) blurred by Gaussian point spread function (figure 4.4(b)) without additive noise (figure 4.4(c)). Figure 4.5 shows the result obtained using the iterative Wiener filter defined by equations (4.2) and (4.3). Figure 4.6 shows the result obtained using Richardson – Lucy algorithm. The results show that the performance of Richardson – Lucy algorithm is much better than the performance of iterative Wiener filter although iterative Wiener filter converges much faster that Richardson – Lucy algorithm. Since blind deconvolution using Richardson – Lucy algorithm provides both reasonable speed and good estimate true image, it is clearly suited for the defect characterization problem in Eddy Current data analysis.

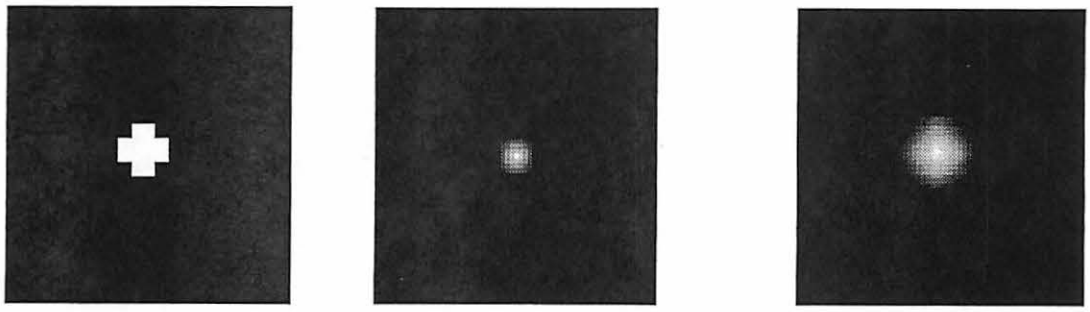

(a) (b) (c)

Figure 4.4 Synthetic images. (a) true image; (b) Gaussian PSF; (c) degraded image.

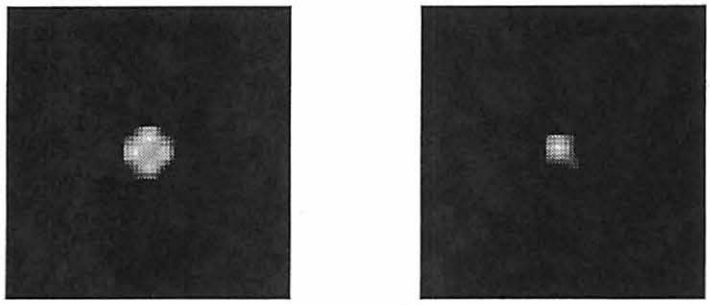

(a) (b)

Figure 4.5 Results using iterative Wiener filter. (a) Estimated true image. (b) Estimated PSF.

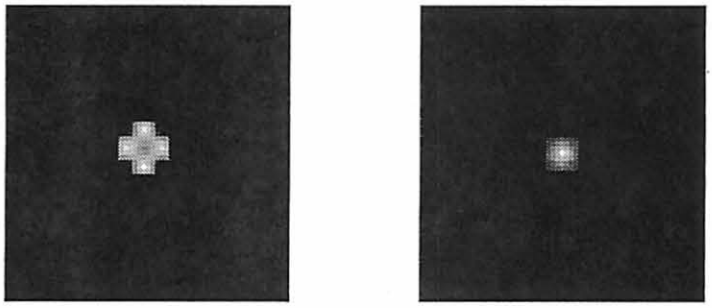

(a) (b)

Figure 4.6 Results using Richardson – Lucy algorithm. (a) Estimated true image. (b) Estimated PSF.

Although Holmes's method is easy to implement, its speed of convergence is often slow. And its failure to achieve reasonable results shows its lack of robustness. To overcome these two disadvantages, Fish, Brinicombe, and Pike [4] proposed another method of implementing the Richardson – Lucy algorithm. In the rth blind iteration, the point spread function $h^r(x,y)$ is estimated by performing a specified number of Richardson – Lucy iterations instead of once as in Holmes's method. Likewise, the original image is estimated by performing the same number of Richardson – Lucy iterations. This method can be summarized as the following two equations:

$$h_{k+1}{}^{r+1}(x,y)=\left\{\left[\frac{g(x,y)}{h_k{}^{r+1}(x,y)\otimes f^r(x,y)}\right]\otimes f^r(-x,-y)\right\}h_k{}^{r+1}(x,y) \qquad (4.21)$$

and

$$f_{k+1}{}^{r+1}(x,y)=\left\{\left[\frac{g(x,y)}{f_k{}^{r+1}(x,y)\otimes h^{r+1}(x,y)}\right]\otimes h^{r+1}(-x,-y)\right\}f_k{}^{r+1}(x,y) \qquad (4.22)$$

where k is the number of Richardson – Lucy iteration. Compared to Holmes's method, Fish's method has a faster speed of convergence and is more robust.

4.6 New Convergence Criteria

Since the blind deconvolution method based on Richardson – Lucy algorithm is in fact an iterative method, choosing an appropriate convergence criterion is important for overall performance. Although Holmes's method and Fish's method can achieve reasonable results, the convergence criterion in these methods have not been fully investigated. This leads to the uncertainty with respect to its robustness.

In the ideal case, the blind deconvolution process should terminate when the estimated true image is identical to the true image. However, the knowledge of true image and the point spread function is often unavailable. The only information accessible is the noisy observed input data. This leads to the difficulty of determining when blind deconvolution should stop. In order to deal with the convergence problem, a new convergence criterion based on mean square error (MSE) is proposed in this section.

In the degradation model used represented by equation (4.1), we assume that the observed image is the convolution of true image and point spread function. Therefore, a error function which is defined to measure the difference between the observed image and the convolution of estimated image $f(x,y)$ and estimated point spread function $h(x,y)$ can be used as the convergence criterion. This error function is based on the mean square error approach and is defined as:

$$E = \frac{1}{N} \sum_{x,y} \left[g(x,y) - f'(x,y) \otimes h'(x,y) \right]^2 \tag{4.23}$$

where N is the total number of pixels in the true image. Equation (4.23) shows that in the absence of additive noise, the mean square error E eventually goes to zero when the estimated true image and estimated point spread function are identical to the true image and true point spread function. In the presence of additive noise, the blind deconvolution process is terminated when error E is less than a predetermine tolerance value.

4.6.1 Modified Richardson – Lucy Algorithm

One advantage that Fish's method has over Holmes's method is that it increases the speed of convergence. However, further improvement can be achieved. Fish's method estimates the point spread function and true image for a given number of Richardson – Lucy iterations in each and every blind iteration. This number is not always the optimal one. In order to make the number of Richardson – Lucy iterations adaptively, an alternate convergence criterion is introduced. In each blind iteration, the number of Richardson – Lucy iteration is calculated based on the following function:

$$C(h_k{}^r(x,y), h_{k-1}{}^r(x,y)) = \frac{\sum_{x,y}\left(h_k{}^r(x,y) - h_{k-1}{}^r(x,y)\right)^2}{\sum_{x,y} h_k{}^r(x,y)^2} \tag{4.24}$$

where r is the number of blind iteration, k is the number of Richardson – Lucy iterations performed in rth blind iteration when estimating the point spread function. C represents the cost function when estimating the point spread function. Figure 4.7 presents the detailed procedures for implementing the proposed new convergence criteria and modified Richardson – Lucy algorithm . When the value of C is less than a predetermine number, the process of estimating point spread function terminates and the number of Richardson – Lucy iterations performed is stored. Then the true image is estimated. The whole blind deconvolution process terminates when the convergence criterion defined in equation 4.23 is satisfied.

Both Fish's method and the method with new convergence criteria were evaluated using synthetic data as well as field data. The results will be presented in chapter 5. Table

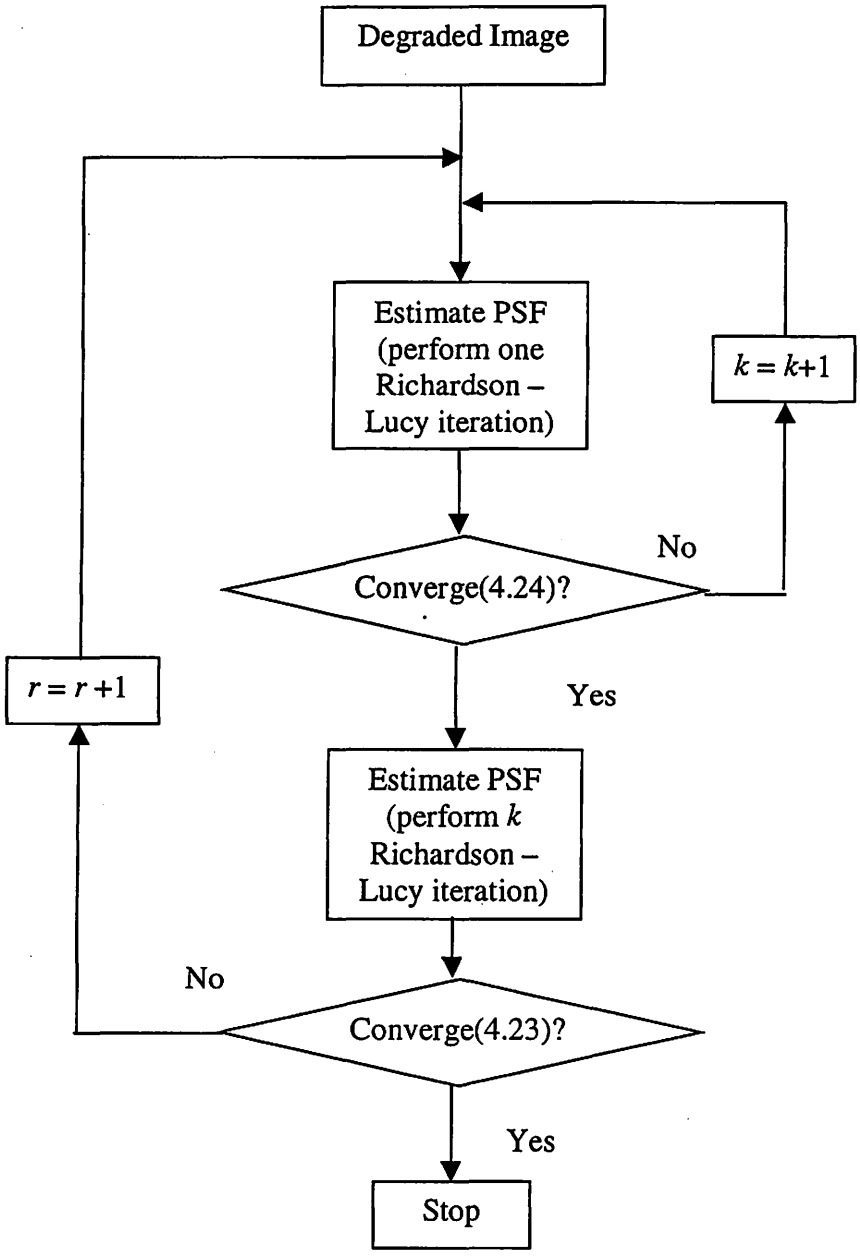

Figure 4.7 Method with new convergence criteria

4.1 summarizes the comparison of convergence speed for Fish's method and the method with new convergence cirteria. The data used include two synthetic images convolved with a Gaussian PSF. Two sets of eddy current data drawn from the calibration tube were also used. Three types of initial estimate for point spread function, namely, random, uniform and Gaussian, are used (the results of blind deconvolution of these data will be presented in chapter 5). The results clearly show that with the proposed algorithm, the speed of convergence of blind deconvolution method is dramatically increased. In some cases, results can be achieved in less than half of the number of iterations used in Fish's method. This leads to lower the overall computational complexity which is critical for practical applications such as steam generator tube inspection in nuclear power plants.

4.7 Application to Defect Characterization of Eddy Current Data

The application of blind deconvolution algorithm to practical eddy current data is not as straightforward as it seems. Figure 4.4 shows an example of typical eddy current data obtained from steam generator tubes in nuclear power plants. The factors that affect the data include variations of probe scanning speed and liftoff. Other changes in the scanning environment can also affect the data. Due to these reasons, the probe response is not invariant during the duration of scanning. However, the probe response is assumed to be invariant locally, which is very reasonable. Therefore, in order to apply blind deconvolution, a small section around the defect signal is chosen as input. This small

Table 4.1 Comparison of speed of convergence between Fish's method and method with new convergence criteria

Defect	Initial Estimate of PSF	Fish's method (No. R-L iter.s)	Method with Conv. (No. R-L iter.s)	
Test data 1 (cross)	Random function	220	106	51.8%
Test data 1 (cross)	Uniform function	180	152	15.6%
Test data 1 (cross)	Gaussian function	140	96	31.4%
Test data 2 (rectangle)	Random function	100	50	50.0%
Test data 2 (rectangle)	Uniform function	50	40	20.0%
Test data 2 (rectangle)	Gaussian function	40	34	15.0%
Defect A (400 kHz)	Random function	30	24	20.0%
Defect A (400 kHz)	Uniform function	30	28	6.7%
Defect A (400 kHz)	Gaussian function	20	12	40.0%
Defect E (300 kHz)	Random function	30	26	13.3%
Defect E (300 kHz)	Uniform function	30	24	20.0%
Defect E (300 kHz)	Gaussian function	20	16	20.0%

Note: Fish's method: Fish's blind deconvolution method;

Method with Conv.: method with new convergence criterion;

No. R-L iter.s: Number of Richardson – Lucy iterations.

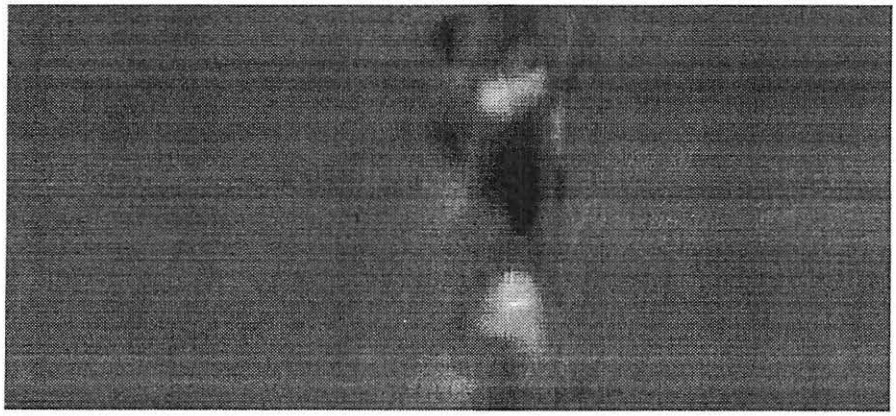

Figure 4.8 A typical eddy current data (Tube NO. DHR006C012I010).

section is called region of interest (ROI). One of the primary objectives of the preprocessing step is to automate the selection of the ROI in Eddy Current C – scan images.

Since defects often occur within the tube support plate (TSP) region the preprocessing is narrowed down to the TSP region. The signal outside the TSP region which is mostly defect free can be used to obtain the statistical parameters that can be used for denoising the signal within the TSP region. The overall approach for defect characterization consists of 3 steps: 1) Preprocessing; 2) Deconvolution; 3) Defect characterization.

For data from any given tube, preprocessing includes the following steps

1. Threshold the data within the TSP region, $d(x,y)$, according to the equation given by

$$\overline{d(x,y)} = \begin{cases} 0 & d(x,y) <= T \\ d(x,y) & d(x,y) > T \end{cases} \tag{4.25}$$

where threshold value T is given by $T = \alpha\sigma$, and σ the standard deviation of the data outside the TSP region, and α is a constant, chosen according to the noise level in the data outside the TSP region. In practice, a value of 2 is chosen for α.

2. Calculate the binary mask function *m(x,y)* from data *d(x,y)* according to the equation given by

$$m(x,y) = \begin{cases} 0 & \overline{d(x,y)} = 0 \\ 1 & \overline{d(x,y)} > 0 \end{cases} \tag{4.26}$$

3. Apply binary morphological operations "closing" and "opening" to *m(x,y).* to obtain the new mask *m'(x,y)* function. This step is used for removing isolated spike noise pixels.
4. The denoised data D(x,y) is obtained according to the following equation

$$D(x,y) = \overline{d(x,y)} \bullet m'(x,y) \tag{4.27}$$

where • denotes the pixel by pixel product.

Figure 4.9 shows the results of performing preprocessing on data obtained from one of the field tubes. Results of preprocessing show significant improvement in the quality of the data without the introduction of any additional distortion.

After preprocessing, an appropriate ROI of data is chosen to be used as input to the blind deconvolution operation. The implementation of the blind deconvolution algorithm,

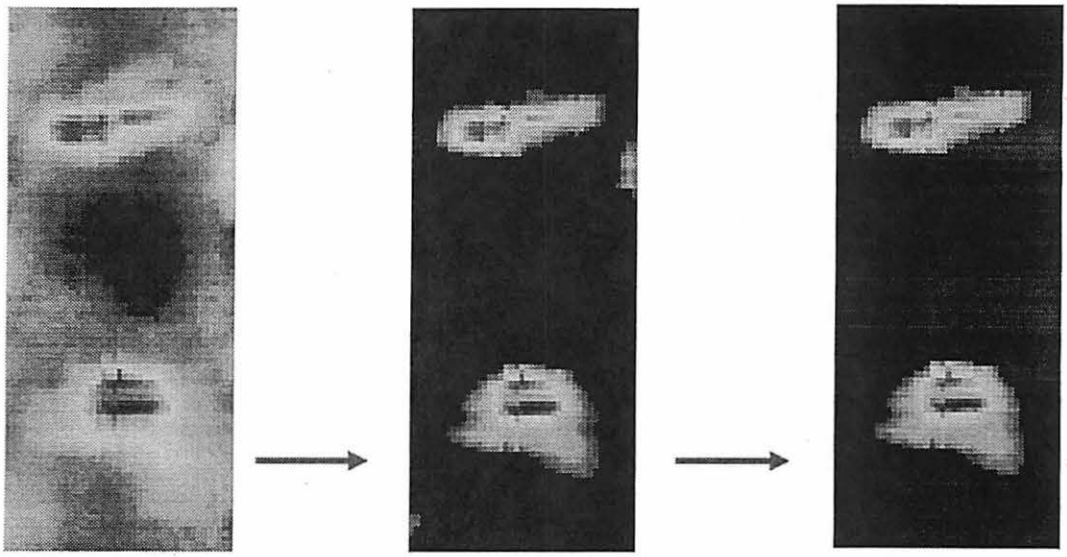

(a) (b) (c)

Figure 4.9 Results of preprocessing (a) Defect signal (b) Signal after thresholding (c) Signal after preprocessing.

described earlier, iteratively estimates the PSF (the kernel) and true image until convergence is achieved. The following steps summarize this procedure:

1. Initialize estimate of probe impulse response/PSF $h(x, y)$ and defect footprint $f(x, y)$.
2. Estimate the new probe response using the measurement $h(x, y)$ according to equation (4.21) and the convergence criterion in equation (4.24). Store the number of Richardson – Lucy iterations.
3. Incorporate the finite support constraint of probe response.

4. Estimate the defect footprint $f(x, y)$ according to equation (4.22) and the number of Richardson – Lucy iterations obtained in step 2.
5. Incorporate the finite support constraint of defect footprint.
6. Repeat steps 2 through 5 until convergence is achieved. The convergence condition is given by equation (4.23).

There are several issues that should be carefully considered in this algorithm:

1. In order to begin the blind deconvolution process, the necessary input information includes the observed data, the initial estimate of probe response $h(x, y)$ and defect footprint $f(x, y)$. Since no detailed knowledge about probe response $h(x, y)$ and defect footprint $f(x, y)$ is available, any choice of initial guess is valid. However the final results of blind deconvolution depend on the initial estimate. Therefore, a careful choice of the initial estimate can certainly improve the performance. Generally, uniform distribution function is used as initial estimate. In steam generator tube inspection, absolute probes are used. From numerical simulation using the finite element model, it is well known that the impulse response/PSF of an absolute probe has a Gaussian shape. Therefore, using a Gaussian function as the initial estimate of probe impulse response $h(x, y)$ instead of uniform distribution can achieve better performance.
2. Since the sampling rates for axial direction and circumferencial direction are often different, it is important to interpolate the data so that the sampling rates

for both directions are the same. This is also critical for generating a reasonable Gaussian distribution data as initial estimate of probe impulse response $h(x, y)$ with known probe diameter. Since the tube support plate always has the length of three quarters of an inch, the sampling rate can be estimated according to the following equation:

$$R = \frac{L}{3/4} \tag{4.28}$$

where R is the sampling rate in the unit of pixels per inch, and L is the length of the tube support plant in number of pixels.

3. The finite support of defect footprint $f(x, y)$ is vital for improving the performance of characterization. In this algorithm, the finite support of $f(x, y)$ is decided according to the support region of defect signal in observed data. In general, the support of $f(x, y)$ is taken as the smallest rectangle that contains the support region of defect signal in observed data.
4. The nonnegativity constraints for defect footprint $f(x, y)$ and probe response $h(x, y)$ do not need to be incorporated separately. They are automatically satisfied in the Richardson – Lucy algorithm as long as the initial estimates of $f(x, y)$ and $h(x, y)$ satisfy nonnegativity constraints.

In next chapter, results of implementing the blind deconvolution method using Richardson – Lucy algorithm are presented. The test EC data includes both calibration

and field data. Different initial estimates of defect footprint $f(x, y)$ and probe impulse response $h(x, y)$ are used and the results are discussed.

CHAPTER 5. RESULTS, CONCLUSION, AND DISCUSSIONS

5.1 Results

The blind deconvolution method described in chapter 4 was implemented on steam generator tube inspection data. Steam generator tube inspection is generally carried out using a bobbin probe or a rotating pancake coil probe. In this work, data was obtained using a rotating pancake coil probe. The calibration tube has an outer diameter of 0.875 inch with both axial and circumferential defects machined. The diameter of the pancake probe is 0.080 inch, and excitation frequencies used are 400 kHz, 300 kHz, and 200 kHz. This method does not perform very well in dealing with the data obtained from bobbin coil. The reason will be discussed later.

First, the algorithm was implemented on synthetic data sets as shown in figures 5.1 – 5.6. The algorithm was implemented next on three sets of data obtained from the calibration tube where the defect information is fully known. The true defect footprint can be generated manually using the available information. Therefore, the results of the blind deconvolution using Richardson – Lucy algorithm can be compared with the true defect footprint to determine the effectiveness of the blind deconvolution method. Figures 5.7 – 5.18 present the results obtained by applying blind deconvolution method to the calibration data. When applying the blind deconvolution method, random, uniform, and Gaussian function were used as the initial guess of probe impulse response.

5.1.1 Results of Synthetic Data Sets

In this section, two synthetic data sets were used to evaluate the performance of blind deconvolution method based on Richardson – Lucy algorithm. The blurred image was generated by "smearing" the synthetic true image using a Gaussian PSF. For each data set, three different initial estimates for PSF were used, namely random, uniform and Gaussian. In each case, results obtained using Fish's method is compared with the results obtained using the method with new convergence criteria.

Figures 5.1, 5.2 and 5.3 present the results for synthetic data set I. The true image is a cross which is shown in figure 5.1 (a). Using a Gaussian PSF shown in figure 5.1 (b), the true image was "smeared" to produce a synthetic measurement which is shown in figure 5.1 (c). This image was then deconvolved using the Richardson – Lucy algorithm. Figures 5.1 (d) and (f) present the results obtained using a random initial estimate of the PSF and figures 5.1 (e) and (g) present the corresponding estimated PSF. Figures 5.2 (a) and (c) present the results obtained using a uniform initial estimate of the PSF, and figures 5.2 (b) and (d) present the corresponding estimated PSF using a uniform initial estimate of the PSF. Figures 5.3 (a) and (c) present the results obtained using a Gaussian initial estimate of the PSF, and figures 5.3 (b) and (d) present the corresponding estimated PSF using a Gaussian initial estimate of the PSF.

The results of all three cases clearly show that initial estimate for PSF has big impact on the final results. The results obtained using Gaussian initial estimate for PSF is seen to yield the best results as expected. Random initial estimate for PSF generated the worst results. Comparing the results obtained using Fish's method and that obtained using the method with new convergence criteria, we can see that both methods performs well for the synthetic data

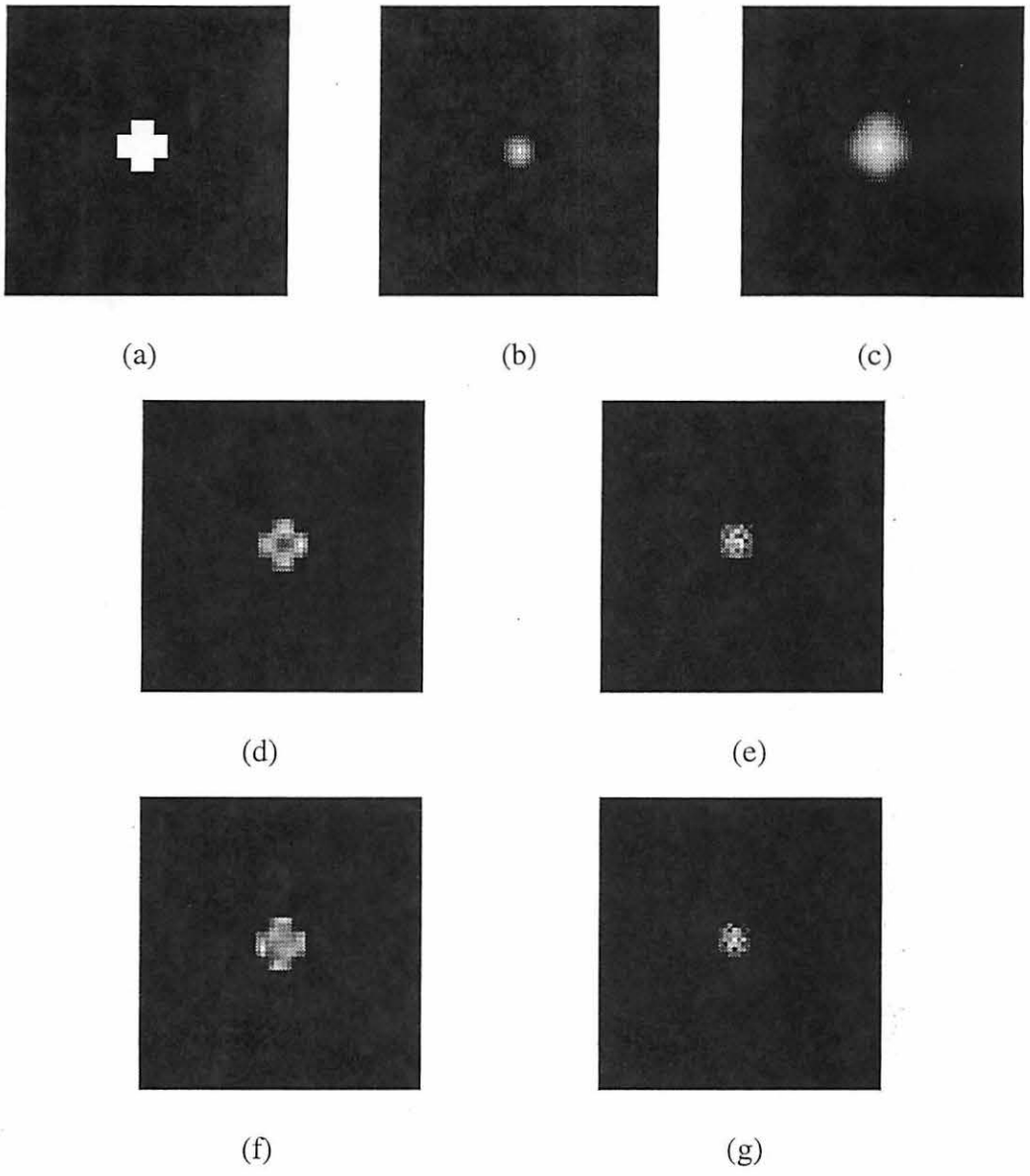

Figure 5.1 Results on synthetic data. (a) True image; (b) Gaussian PSF; (c) Observed image; (d) Deconvolved image using random initial estimate of PSF(Fish, after 220 R – L iterations); (e) Estimated PSF using random initial estimate of PSF(Fish); (f) Deconvolved image using random initial estimate of PSF(new convergence criteria, after 106 R – L iterations); (g) Estimated PSF using random initial estimate of PSF (new convergence criteria)

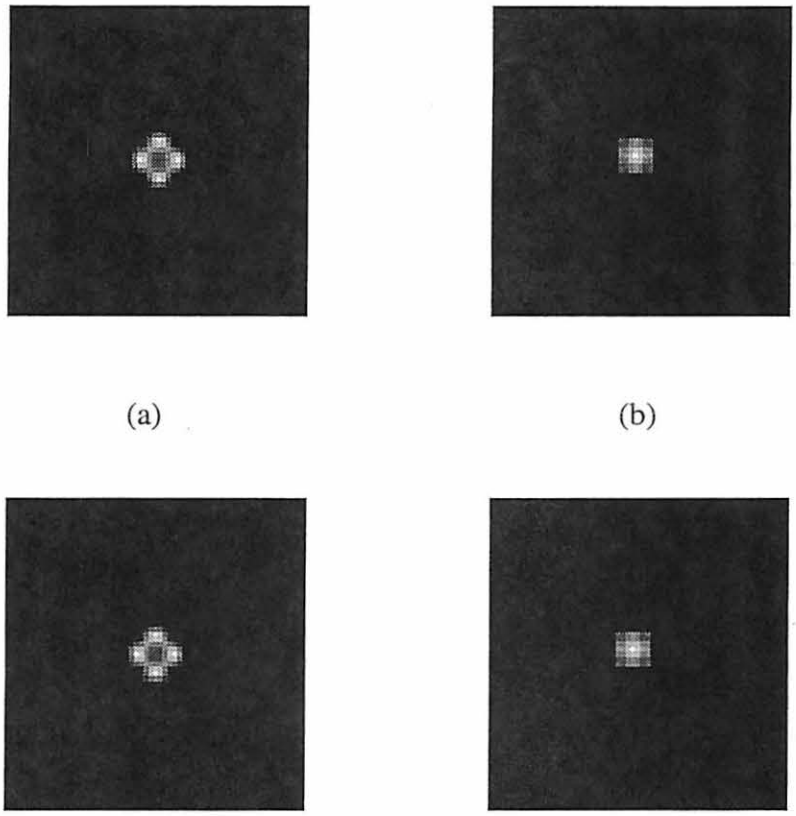

(a) (b)

(c) (d)

Figure 5.2 Results on synthetic data in Figure 5.1(c). (a) Deconvolved image using uniform initial estimate of PSF(Fish, after 180 R – L iterations); (b) Estimated PSF using uniform initial estimate of PSF(Fish); (c) Deconvolved image using uniform initial estimate of PSF(new convergence criteria, after 152 R – L iterations); (d) Estimated PSF using uniform initial estimate of PSF (new convergence criteria)

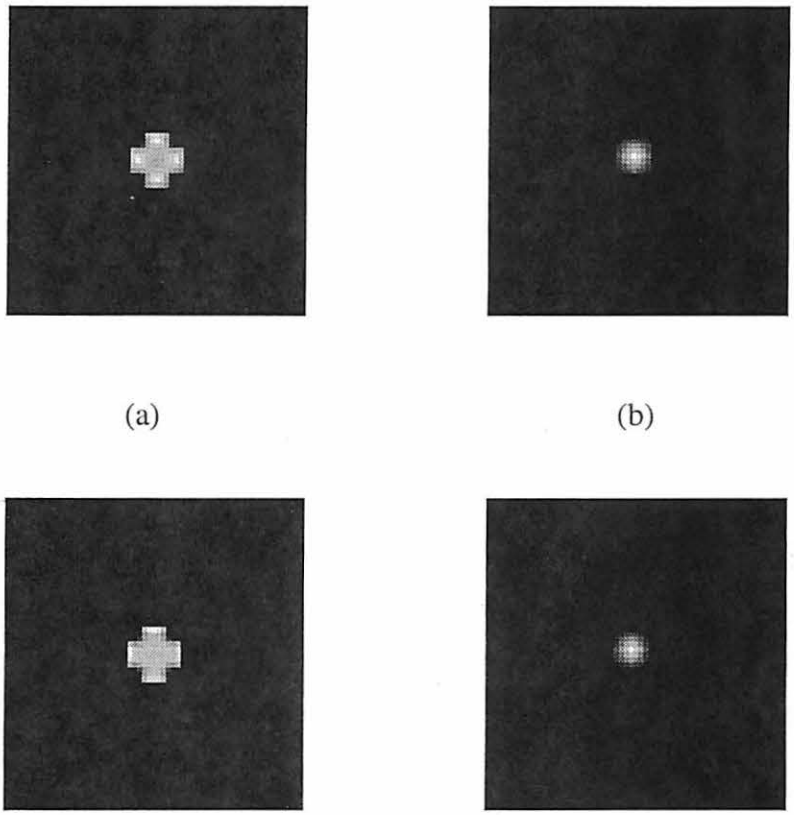

(a) (b)

(c) (d)

Figure 5.3 Results on synthetic data in Figure 5.1(c). (a) Estimated image using Gaussian initial estimate for PSF(Fish, after 140 R – L iterations); (b) Estimated PSF using Gaussian initial estimate of PSF(new convergence criteria); (c) Deconvolved image using Gaussian initial estimate for PSF (new convergence criteria, after 96 R – L iterations); (d)Estimated PSF using Gaussian initial estimate of PSF (new convergence criteria)

set. Although the method with new convergence criteria doesn't dramatically improve the final results, it does save the computational time which is critical in practical applications.

Figures 5.4, 5.5 and 5.6 present the results for synthetic data set I. The true image is a rectangle which is shown in figure 5.4 (a). Using a Gaussian PSF shown in figure 5.4 (b), the true image was "smeared" to produce a synthetic measurement which is shown in figure 5.4 (c). This image was then deconvolved using the Richardson – Lucy algorithm. Figures 5.4 (d) and (f) present the results obtained using a random initial estimate of the PSF and figures 5.4 (e) and (g) present the corresponding estimated PSF using a random initial estimate of the PSF. Figures 5.5 (a) and (c) present the results obtained using a uniform initial estimate of the PSF, and figures 5.5 (b) and (d) present the corresponding estimated PSF using a uniform initial estimate of the PSF. Figures 5.6 (a) and (c) present the results obtained using a Gaussian initial estimate of the PSF, and figures 5.6 (b) and (d) present the corresponding estimated PSF using a Gaussian initial estimate of the PSF.

The results of all three cases clearly show that initial estimate of PSF has big impact on the final results. The results obtained using Gaussian initial estimate of PSF is seen to yield the best results as expected. Random initial estimate of PSF generated the worst results. Comparing the results obtained using Fish's method and that obtained using the method with new convergence criteria, we can see that both methods performs well for the synthetic data set. Although the method with new convergence criteria doesn't dramatically improve the final results, it does save the computational time which is critical in practical applications.

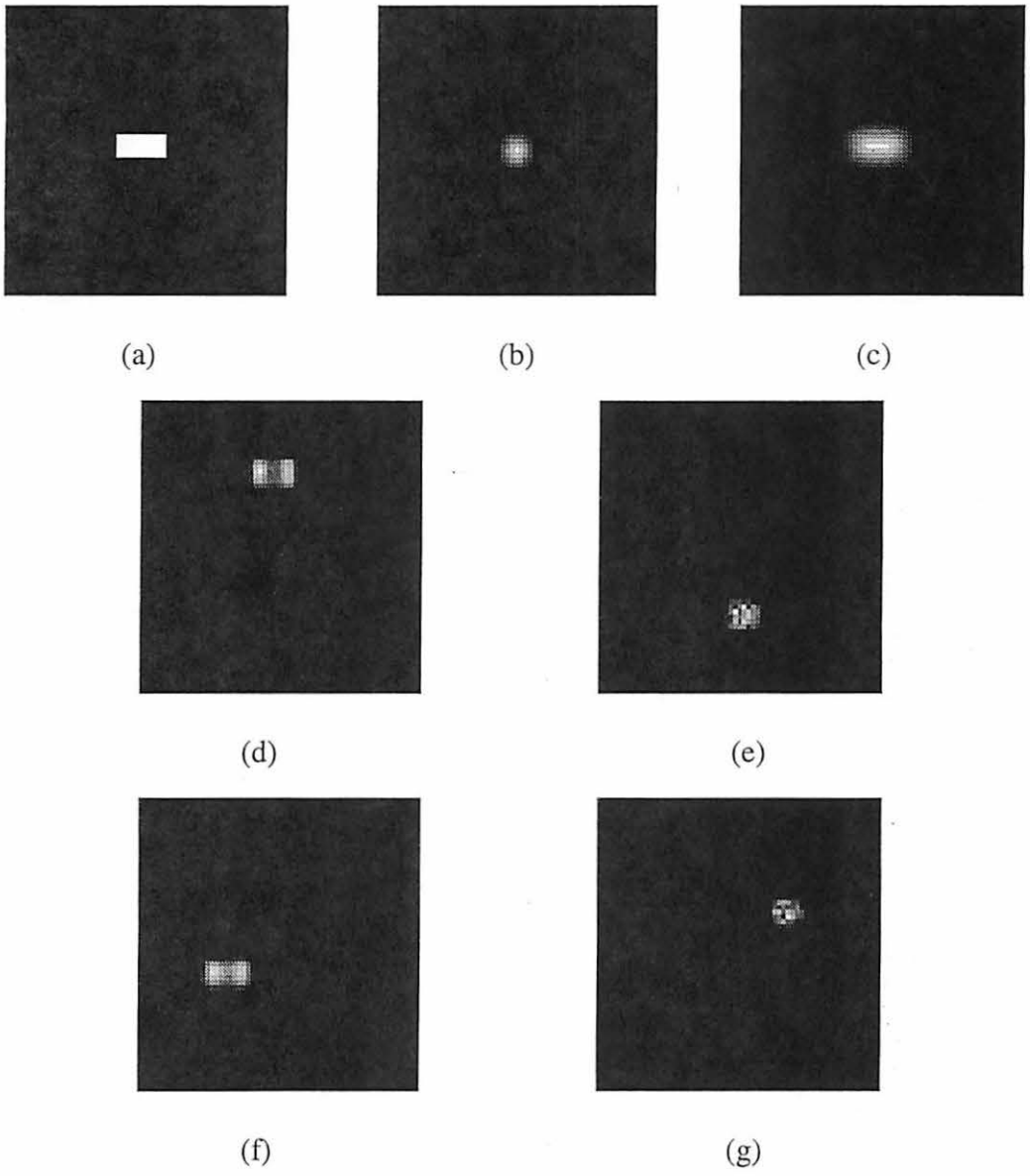

Figure 5.4 Results on synthetic data. (a) True image; (b) Gaussian PSF; (c) Observed image; (d) Deconvolved image using random initial estimate of PSF(Fish, after 100 R – L iterations); (e) Estimated PSF using random initial estimate of PSF(Fish); (f) Deconvolved image using random initial estimate of PSF(new convergence criteria, after 50 R – L iterations); (g) Estimated PSF using random initial estimate of PSF (new convergence criteria)

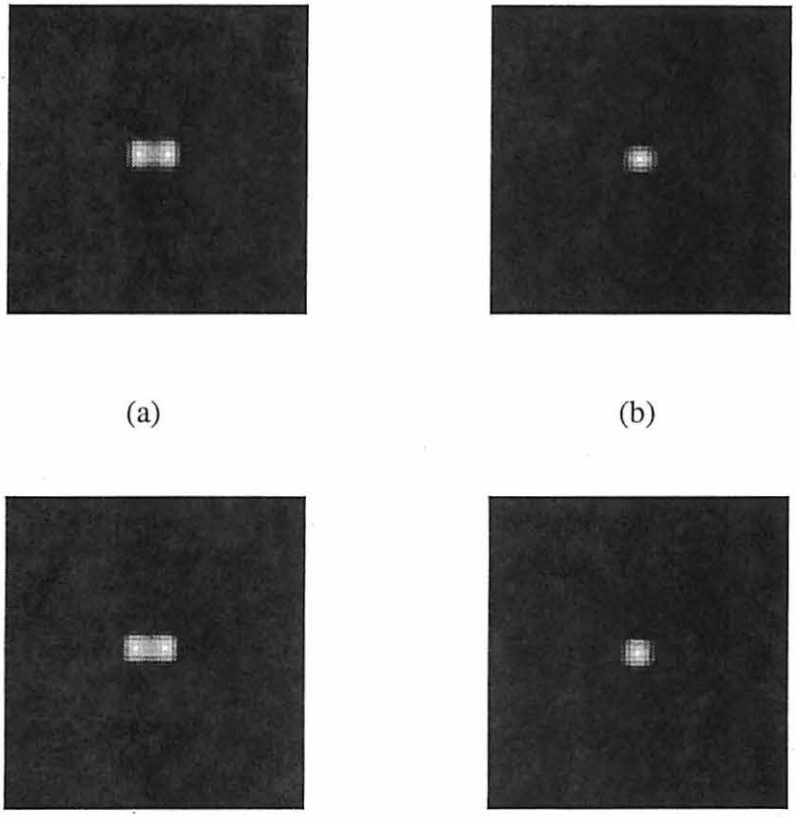

(a) (b)

(c) (d)

Figure 5.5 Results on synthetic data in Figure 5.1(c). (a) Deconvolved image using uniform initial estimate of PSF(Fish, after 50 R – L iterations); (b) Estimated PSF using uniform initial estimate of PSF(Fish); (c) Deconvolved image using uniform initial estimate of PSF(new convergence criteria, after 40 R – L iterations); (d) Estimated PSF using uniform initial estimate of PSF (new convergence criteria)

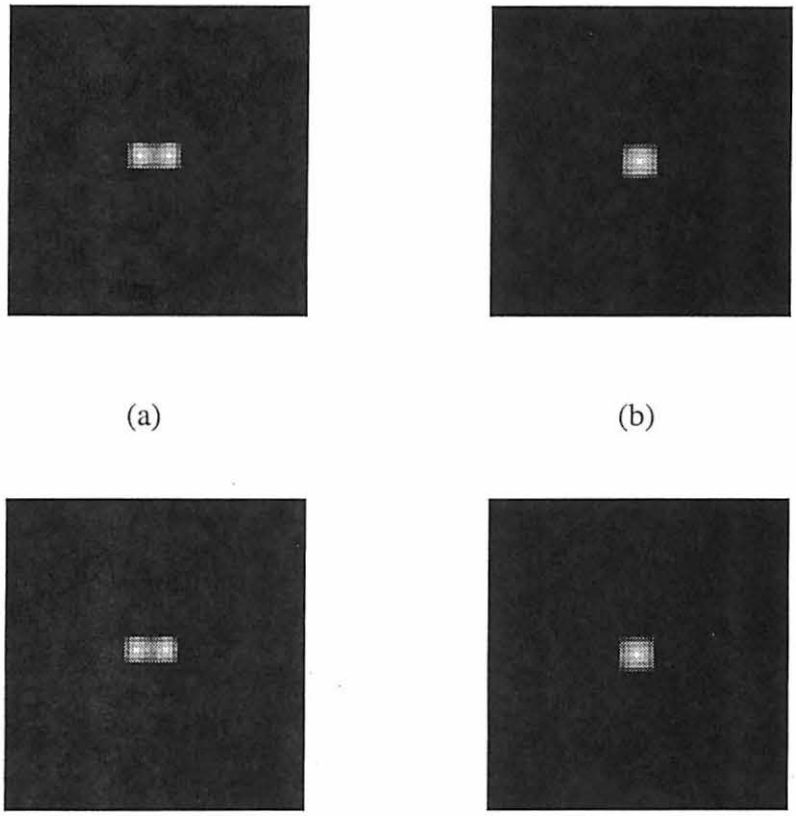

(a) (b)

(c) (d)

Figure 5.6 Results on synthetic data in Figure 5.1(c). (a) Estimated image using Gaussian initial estimate for PSF(Fish, after 40 R – L iterations); (b) Estimated PSF using Gaussian initial estimate of PSF(new convergence criteria); (c) Deconvolved image using Gaussian initial estimate for PSF (new convergence criteria, after 34 R – L iterations); (d)Estimated PSF using Gaussian initial estimate of PSF (new convergence criteria)

5.1.2 Results of Calibration Data

In this section, three calibration data sets were used to evaluate the performance of the blind deconvolution method based on Richardson – Lucy algorithm. The calibration tube has an outer diameter of 0.875 inch with both axial and circumferential defects machined. The diameter of the pancake probe is 0.080 inch, and excitation frequencies used are 400 kHz, 300 kHz, and 200 kHz. For each data set, three types of initial estimates of probe PSF were used, namely random, uniform and Gaussian. In each case, both Fish's method and the method with the new convergence criteria were studied.

Figures 5.7, 5.8 and 5.9 present the results for calibration data set A for an axial defect of length 0.50". The observed raw data is shown in figure 5.7 (a), the data after 3dB thresholding is shown in figure 5.7 (b), and the true defect image is shown in figure 5.7 (c). This raw data was then deconvolved using the Richardson – Lucy algorithm. Figures 5.7 (d) and (f) present the results obtained using a random initial estimate of the PSF, and figures 5.7 (e) and (g) present the corresponding estimated PSF using a random initial estimate of the PSF. Figures 5.8 (a) and (c) present the results obtained using a uniform initial estimate of the PSF, and figures 5.8 (b) and (d) present the corresponding estimated PSF using a uniform initial estimate of the PSF. Figures 5.9 (a) and (c) present the results obtained using a Gaussian initial estimate of the PSF, and figures 5.9 (b) and (d) present the corresponding estimated PSF using a Gaussian initial estimate of the PSF. Figure 5.10 presents the one dimensional cross section of results on defect A.

The results in all three cases again show that initial estimate of PSF has a big impact on the final results. The results obtained using Gaussian initial estimate of PSF are slightly better than the results obtained using uniform and random initial estimate of PSF. Compared

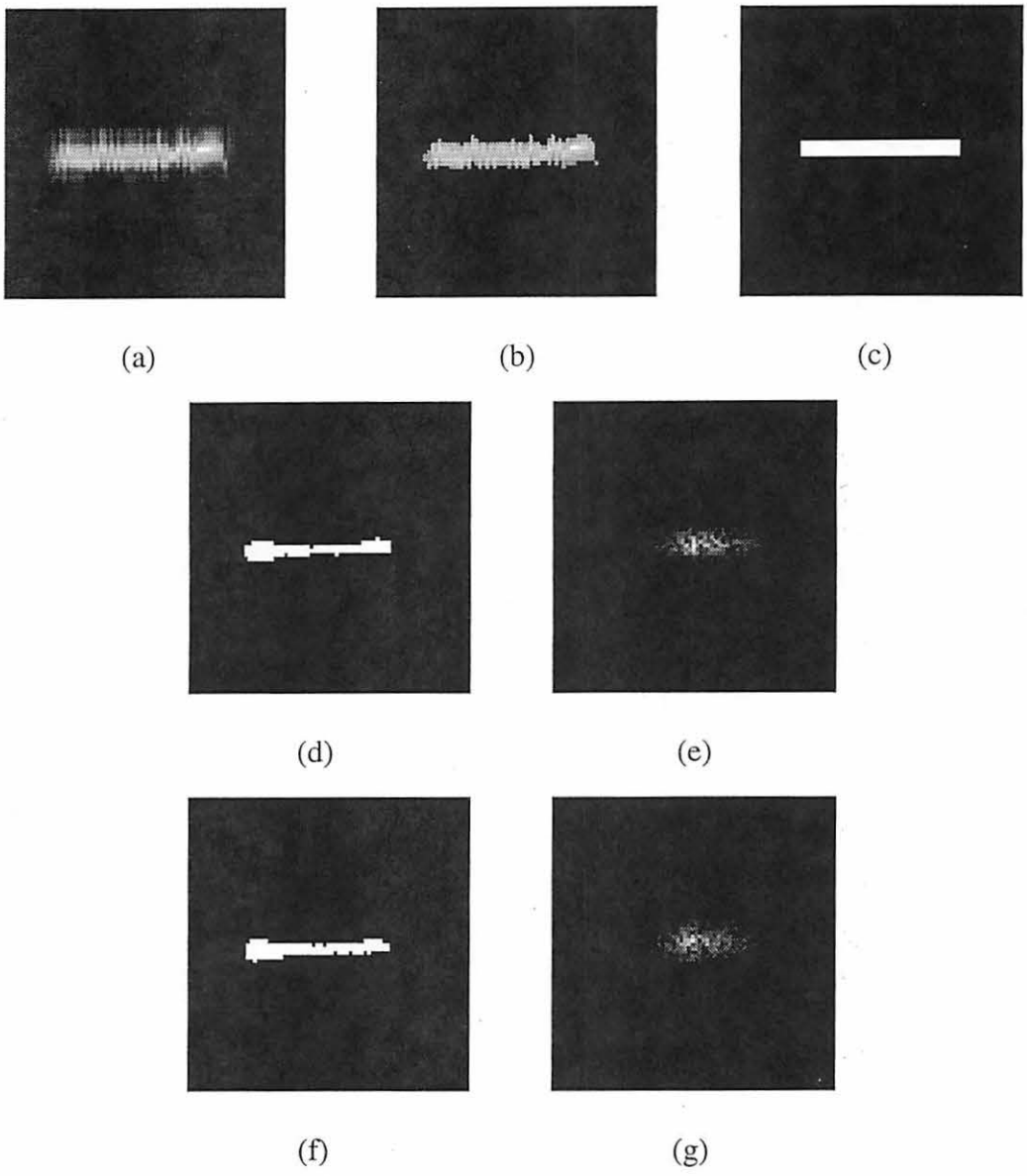

Figure 5.7 Results on calibration data from defect A, excitation frequency: 400 kHz; (a) Raw data; (b) Raw data after 3dB thresholding; (c) True defect profile; (d) Deconvolved defect profile using random initial estimate of PSF (Fish, after 30 R – L iterations); (e) Estimated PSF using random initial estimate of PSF (Fish); (f) Deconvolved defect profile using random initial estimate of PSF (new convergence criteria, after 24 R – L iterations); (g) Estimate PSF using random initial estimate of PSF (new convergence criteria)

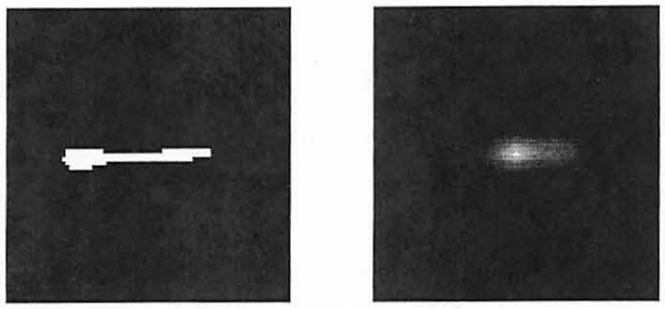

(a) (b)

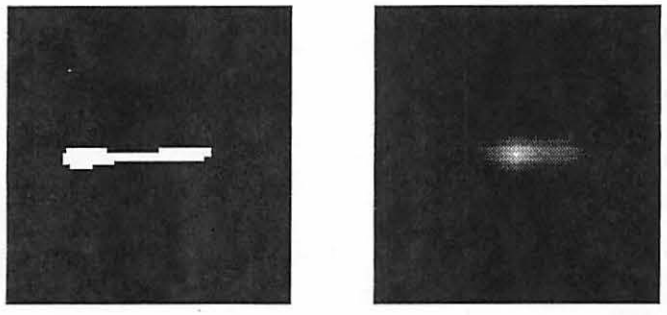

(c) (d)

Figure 5.8 Results on calibration data from defect A, excitation frequency: 400 kHz; (a) Deconvolved defect profile using uniform initial estimate of PSF (Fish, after 30 R – L iterations); (b) Estimated PSF using uniform initial estimate of PSF (Fish); (c) Deconvolved defect profile using uniform initial estimate of PSF (new convergence criteria, after 28 R – L iterations); (d) Estimated PSF using uniform initial estimate of PSF (new convergence criteria)

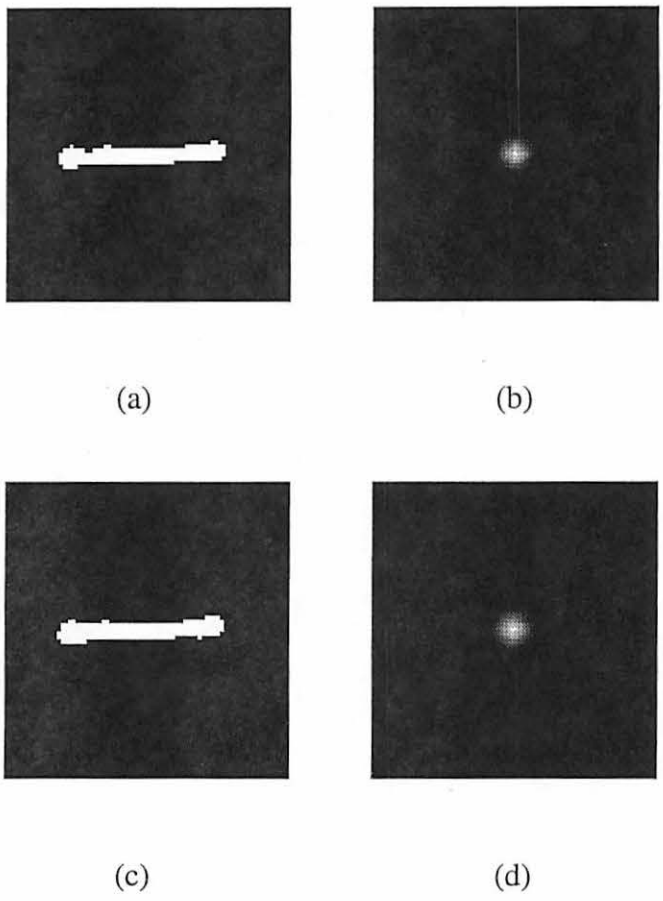

(a) (b)

(c) (d)

Figure 5.9 Results on calibration data from defect A, excitation frequency: 400 kHz; (a) Deconvolved defect profile using Gaussian initial estimate of PSF (Fish, after 20 R – L iterations); (b) Estimated PSF using Gaussian initial estimate of PSF (Fish); (c) Deconvolved defect profile using Gaussian initial estimate of PSF (new convergence criteria, after 12 R – L iterations); (d) Estimated PSF using Gaussian initial estimate of PSF (new convergence criteria)

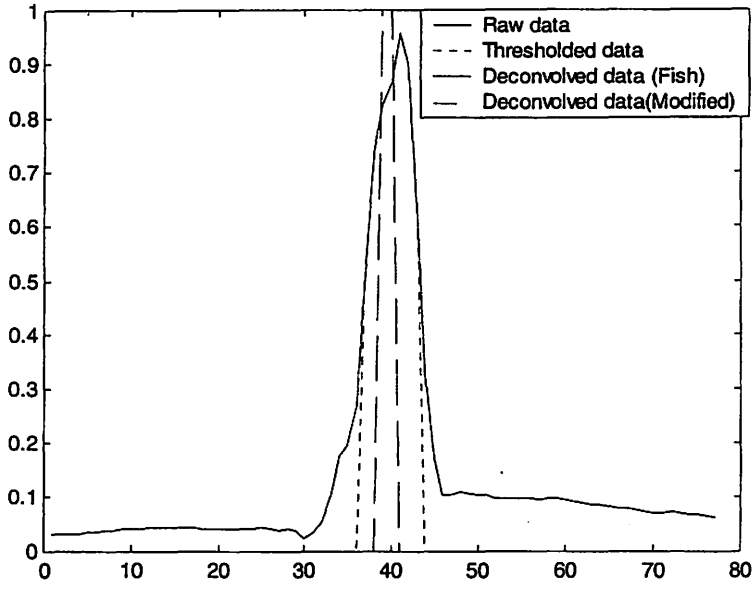

(a)

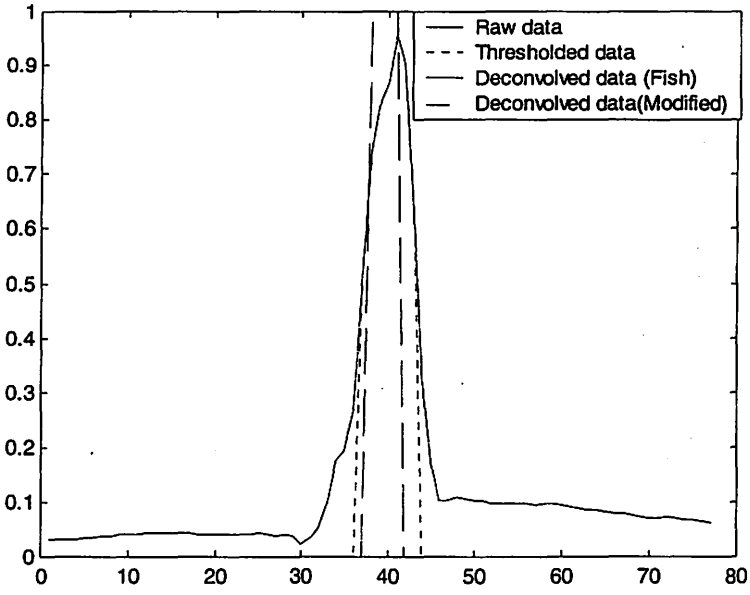

(b)

Figure 5.10 One dimensional cross section of results on defect A. (a) Results obtained using uniform initial estimate of PSF; (b) Results obtained using Gaussian initial estimate of PSF.

the results obtained by using Fish's method and the method with new convergence criteria, we can see that both methods performs well on the calibration data set. Although the method with new convergence criteria does not dramatically improve the final results, it offers savings in computational time.

Figures 5.11, 5.12 and 5.13 present the results for calibration data set E for a circumferential defect of length 0.50". The observed raw data is shown in figure 5.11 (a), the data after 3dB thresholding is shown in figure 5.11 (b), and the true defect image is shown in figure 5.11 (c). This raw data was then deconvolved using the Richardson – Lucy algorithm. Figures 5.11 (d) and (f) present the results obtained using a random initial estimate of the PSF, and figures 5.11 (e) and (g) present the corresponding estimated PSF using a random initial estimate of the PSF. Figures 5.12 (a) and (c) present the results obtained using a uniform initial estimate of the PSF, and figures 5.12 (b) and (d) present the corresponding estimated PSF using a uniform initial estimate of the PSF. Figures 5.13 (a) and (c) present the results obtained using a Gaussian initial estimate of the PSF, and figures 5.13 (b) and (d) present the corresponding estimated PSF using a Gaussian initial estimate of PSF. Figure 5.14 present the one dimensional cross section of results on defect E.

The results in all three cases again show that initial estimate of PSF has a big impact on the final results. The results obtained using Gaussian initial estimate of PSF are slightly better than the results obtained using uniform and random initial estimate of PSF. Compared the results obtained by using Fish's method and the method with new convergence criteria, we can see that both methods performs well on the calibration data set. Although the method with new convergence criteria does not dramatically improve the final results, it offers savings in computational time.

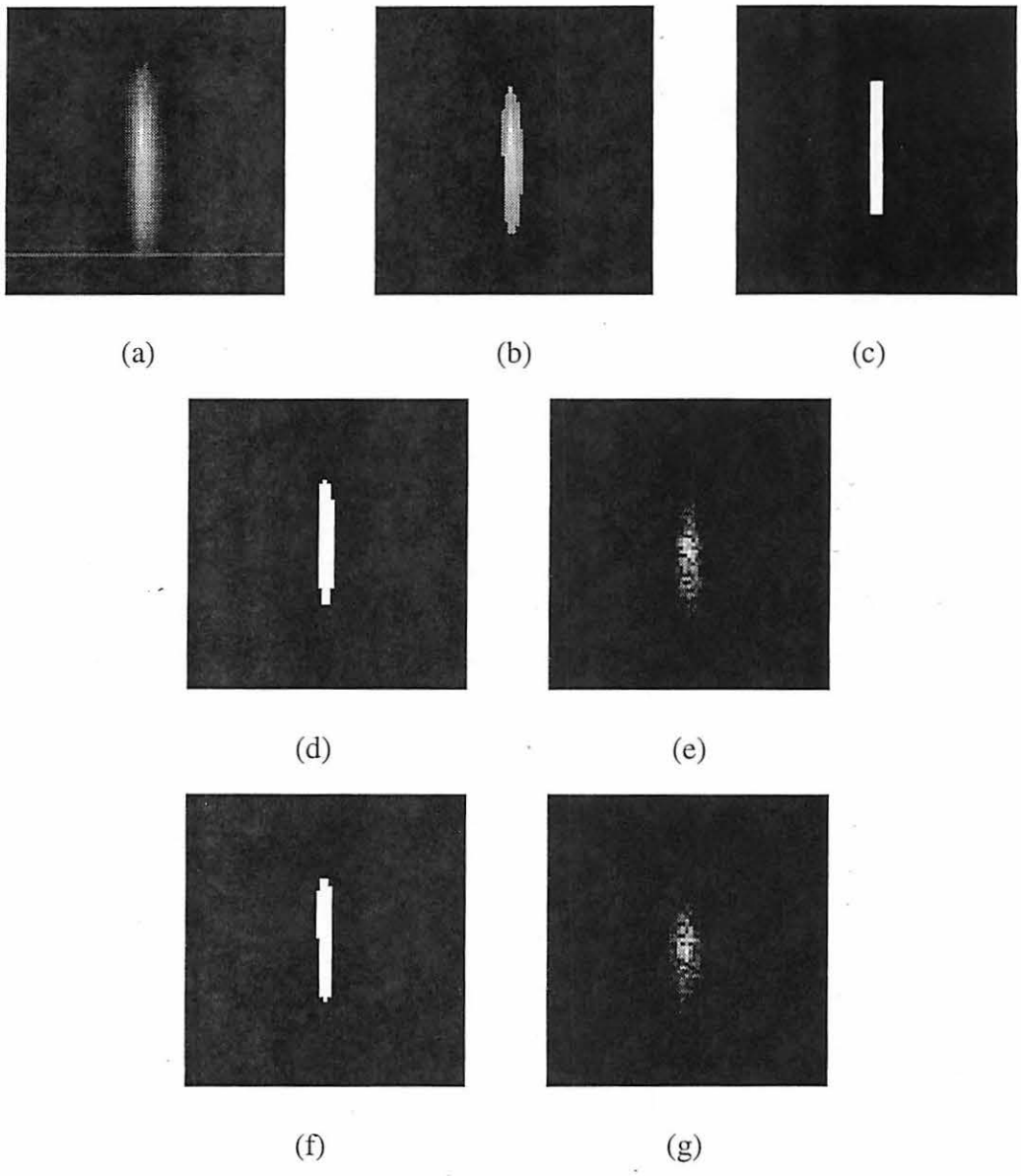

Figure 5.11 Results on calibration data from defect E, excitation frequency: 300 kHz; (a) Raw data; (b) Raw data after 3dB thresholding; (c) True defect profile; (d) Deconvolved defect profile using random initial estimate of PSF (Fish, after 30 R – L iterations); (e) Estimated PSF using random initial estimate of PSF (Fish); (f) Deconvolved defect profile using random initial estimate of PSF (new convergence criteria, after 26 R – L iterations); (g) Estimate PSF using random initial estimate of PSF (new convergence criteria)

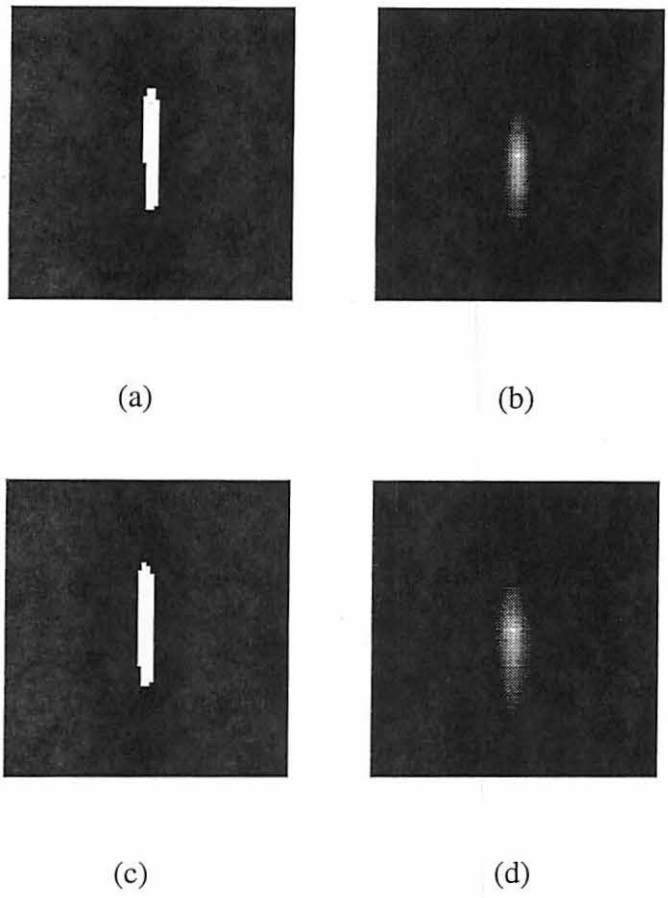

(a) (b)

(c) (d)

Figure 5.12 Results on calibration data from defect E, excitation frequency: 300 kHz; (a) Deconvolved defect profile using uniform initial estimate of PSF (Fish, after 30 R – L iterations); (b) Estimated PSF using uniform initial estimate of PSF (Fish); (c) Deconvolved defect profile using uniform initial estimate of PSF (new convergence criteria, after 24 R – L iterations); (d) Estimated PSF using uniform initial estimate of PSF (new convergence criteria)

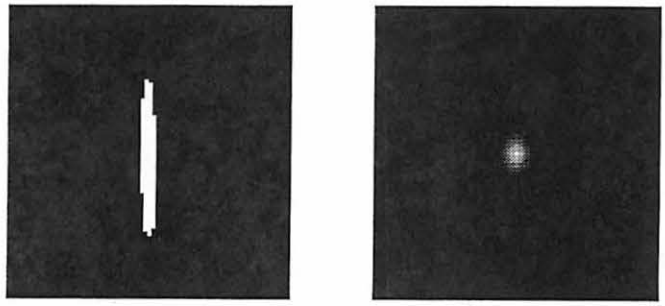

(a) (b)

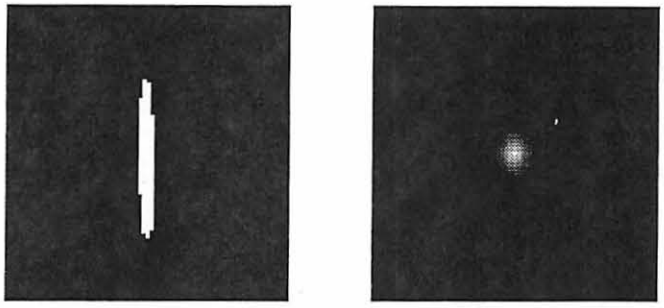

(c) (d)

Figure 5.13 Results on calibration data from defect E, excitation frequency: 300 kHz; (a) Deconvolved defect profile using Gaussian initial estimate of PSF (Fish, after 20 R – L iterations); (b) Estimated PSF using Gaussian initial estimate of PSF (Fish); (c) Deconvolved defect profile using Gaussian initial estimate of PSF (new convergence criteria, after 16 R – L iterations); (d) Estimated PSF using Gaussian initial estimate of PSF (new convergence criteria)

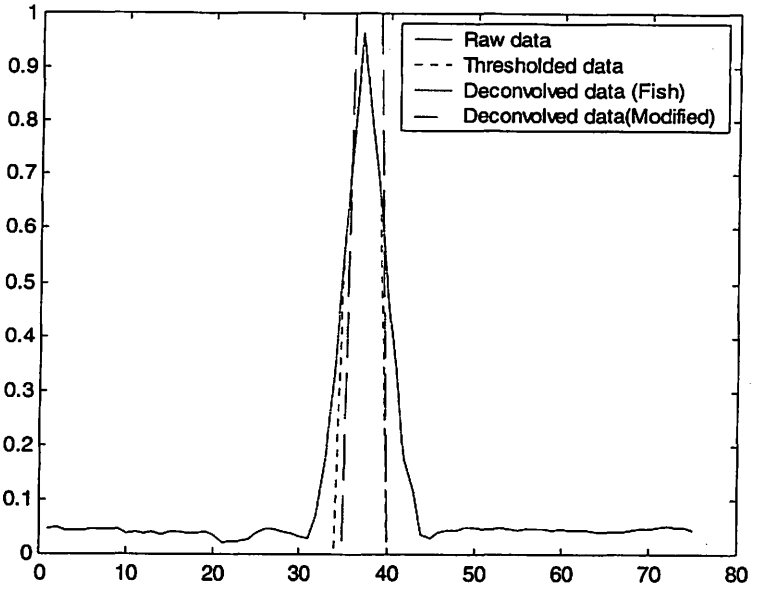

(a)

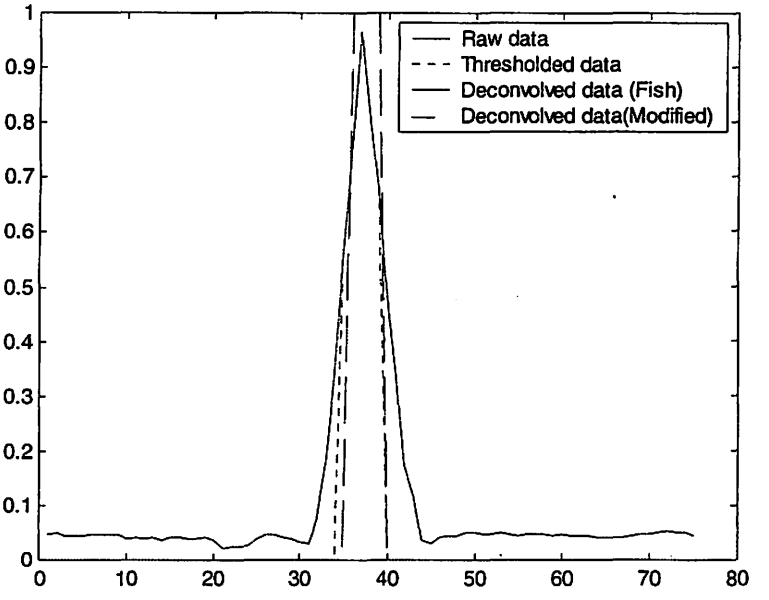

(b)

Figure 5.14 One dimensional cross section of results on defect E. (a) Results obtained using uniform initial estimate of PSF; (b) Results obtained using Gaussian initial estimate of PSF.

Figures 5.15, 5.16 and 5.17 present the results for calibration data set F for an axial defect of length 0.50". The observed raw data is shown in figure 5.15 (a), the data after 3dB thresholding is shown in figure 5.15 (b), and the true defect image is shown in figure 5.15 (c). This raw data was then deconvolved using the Richardson – Lucy algorithm. Figures 5.15 (d) and (f) present the results obtained using a random initial estimate of the PSF, and figures 5.15 (e) and (g) present the corresponding estimated PSF using a random initial estimate of the PSF. Figures 5.16 (a) and (c) present the results obtained using a uniform initial estimate of the PSF, and figures 5.16 (b) and (d) present the corresponding estimated PSF using a uniform initial estimate of the PSF. Figures 5.17 (a) and (c) present the results obtained using a Gaussian initial estimate of the PSF, and figures 5.17 (b) and (d) present the corresponding estimated PSF using a Gaussian initial estimate of PSF. Figure 5.18 present the one dimensional cross section of results on defect F.

The results in all three cases again show that initial estimate of PSF has a big impact on the final results. The results obtained using Gaussian initial estimate of PSF are slightly better than the results obtained using uniform and random initial estimate of PSF. Compared the results obtained by using Fish's method and the method with new convergence criteria, we can see that both methods performs well on the calibration data set. Although the method with new convergence criteria does not dramatically improve the final results, it offers savings in computational time.

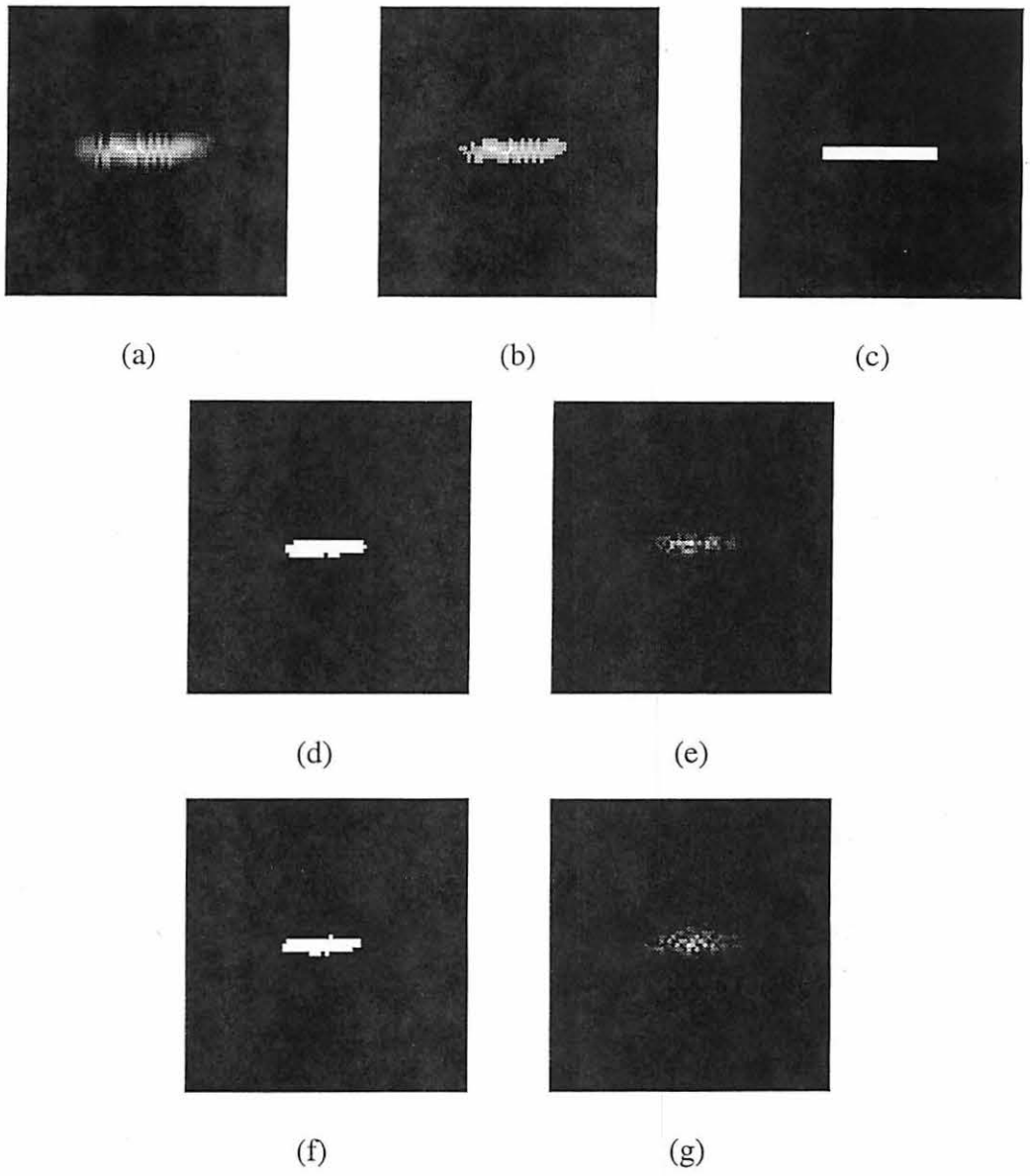

Figure 5.15 Results on calibration data from defect F, excitation frequency: 200 kHz; (a) Raw data; (b) Raw data after 3dB thresholding; (c) True defect profile; (d) Deconvolved defect profile using random initial estimate of PSF (Fish, after 30 R – L iterations); (e) Estimated PSF using random initial estimate of PSF (Fish); (f) Deconvolved defect profile using random initial estimate of PSF (new convergence criteria, after 24 R – L iterations); (g) Estimate PSF using random initial estimate of PSF (new convergence criteria)

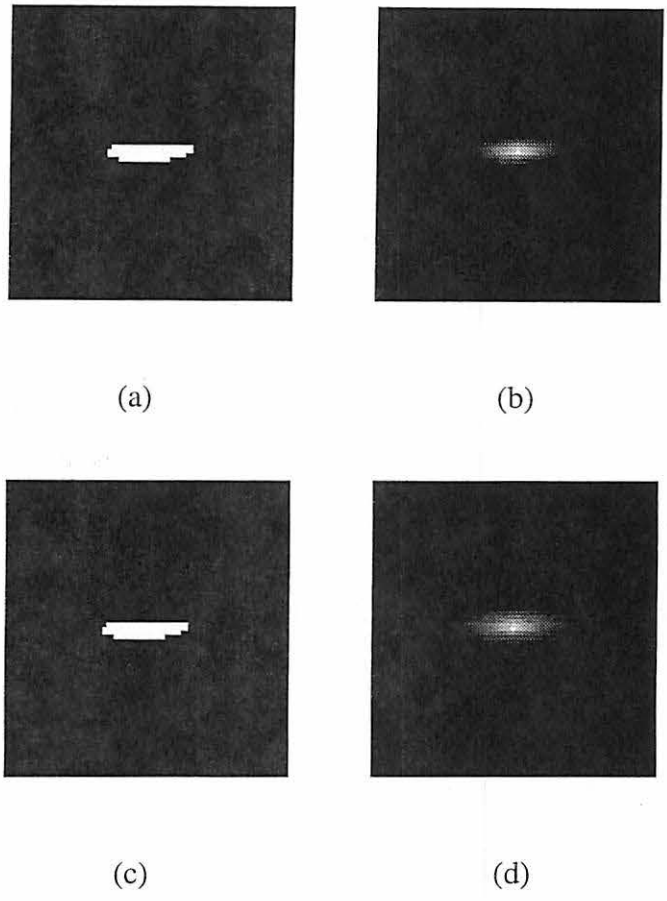

(a) (b)

(c) (d)

Figure 5.16 Results on calibration data from defect F, excitation frequency: 200 kHz; (a) Deconvolved defect profile using uniform initial estimate of PSF (Fish, after 30 R – L iterations); (b) Estimated PSF using uniform initial estimate of PSF (Fish); (c) Deconvolved defect profile using uniform initial estimate of PSF (new convergence criteria, after 24 R – L iterations); (d) Estimated PSF using uniform initial estimate of PSF (new convergence criteria)

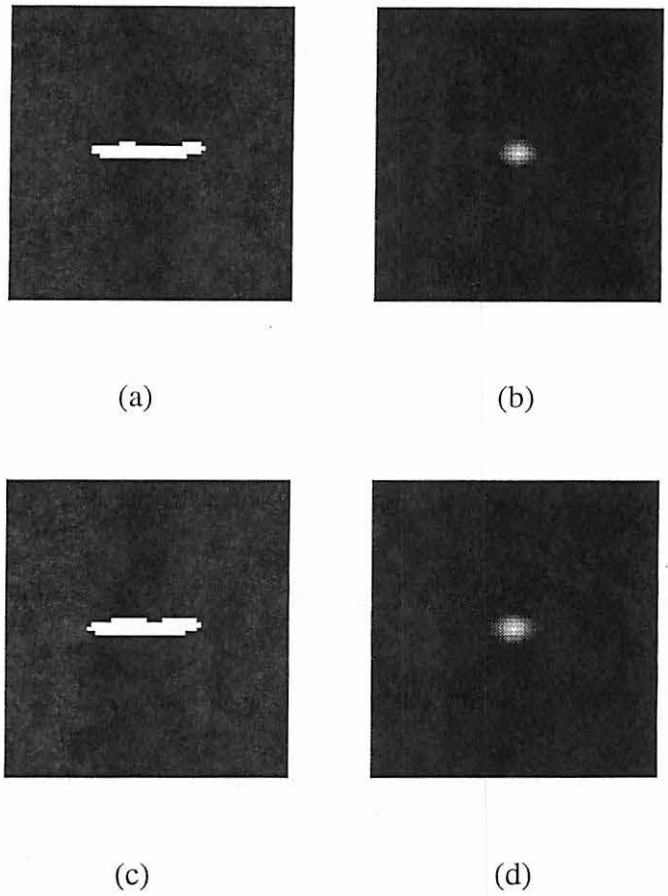

(a) (b)

(c) (d)

Figure 5.17 Results on calibration data from defect F, excitation frequency: 200 kHz; (a) Deconvolved defect profile using Gaussian initial estimate of PSF (Fish, after 20 R – L iterations); (b) Estimated PSF using Gaussian initial estimate of PSF (Fish); (c) Deconvolved defect profile using Gaussian initial estimate of PSF (new convergence criteria, after 14 R – L iterations); (d) Estimated PSF using Gaussian initial estimate of PSF (new convergence criteria)

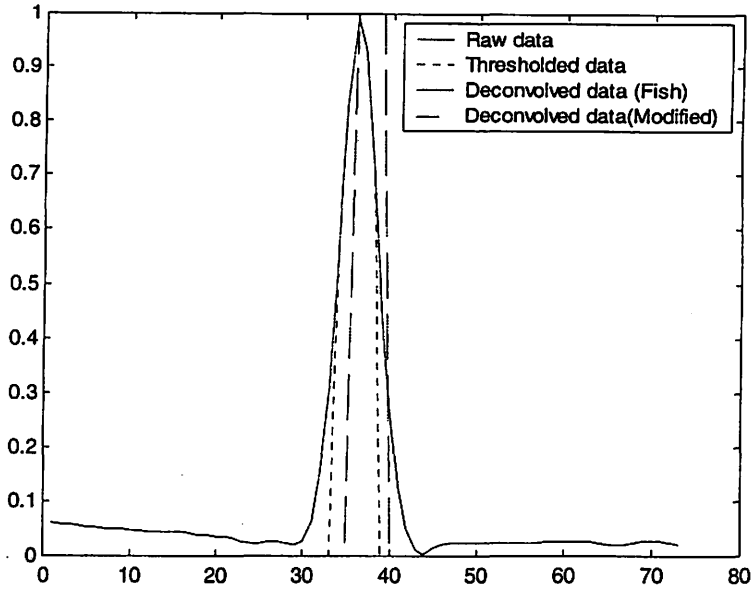

(a)

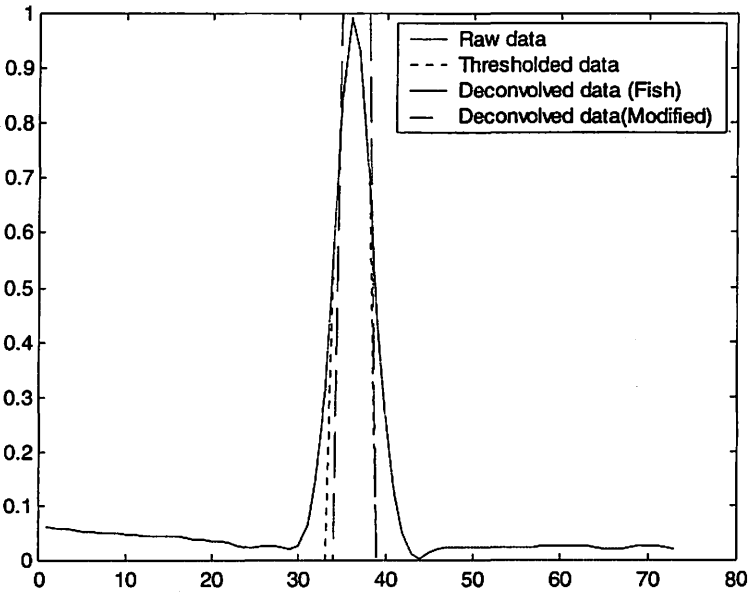

(b)

Figure 5.18 One dimensional cross section of results on defect F. (a) Results obtained using uniform initial estimate of PSF; (b) Results obtained using Gaussian initial estimate of PSF.

Results presented so far show that the blind deconvolution method using Richardson – Lucy algorithm performs very well for the synthetic data as well as the eddy current data obtained from the calibration tube. Results obtained using different initial estimates of the point spread function (see table 5.1) show that the initial estimate for PSF has great impact on the final estimate of the true defect profile. In the case of rotating absolute pancake coil probe, choosing a Gaussian function as the initial estimate of the point spread function yields best performance.

Also worth noting is that the method with new convergence criterion does not dramatically improve the final results, but it saves a considerable amount of computing time. Therefore, it can successfully lower the level of computational complexity which is very critical in steam generator tube inspection in nuclear power plants.

In order to further evaluate this method, field data obtained from the tubes used in steam generators in nuclear power plants were used to test the blind deconvolution method. One problem in using field data is that it is hard to compare the results with the true defect footprint since knowledge of the true defect footprint is not usually available. The results of applying blind deconvolution method on three sets of field data are presented in the following section.

5.1.3 Results on Field Data

In this section, three field data sets were used to evaluate the performance of blind deconvolution method based on Richardson – Lucy algorithm. The field data were obtain in steam generator tube inspection in nuclear power plants using the pancake coil probe of diameter 0.0875 inch, and excitation frequencies used were 400 kHz, 300 kHz, and 200 kHz.

Table 5.1 Comparison of estimate defect surface profile using different initial estimate of PSF

Defect	Initial Estimate of PSF	Method	Length of estimate defect (inch)	Error
Defect A in Calibration tube, excitation frequency 400 kHz, length of true defect is 0.50"	Random function	Fish *et al.*'s	0.45	10.0%
		New Conv. Crit.	0.44	12.0%
	Uniform function	Fish *et al.*'s	0.45	10.0%
		New Conv. Crit.	0.45	10.0%
	Gaussian function	Fish *et al.*'s	0.51	2%
		New Conv. Crit.	0.51	2%
Defect E in Calibration tube, excitation frequency 300 kHz, length of true defect is 0.50"	Random function	Fish *et al.*'s	0.44	12.0%
		New Conv. Crit.	0.43	14.0%
	Uniform function	Fish *et al.*'s	0.43	14.0%
		New Conv. Crit.	0.44	12.0%
	Gaussian function	Fish *et al.*'s	0.52	4.0%
		New Conv. Crit.	0.52	4.0%
Defect F in Calibration tube, excitation frequency 200 kHz, length of true defect is 0.50"	Random function	Fish *et al.*'s	0.41	18.0%
		New Conv. Crit.	0.39	22.0%
	Uniform function	Fish *et al.*'s	0.43	14.0%
		New Conv. Crit.	0.43	14.0%
	Gaussian function	Fish *et al.*'s	0.53	6.0%
		New Conv. Crit.	0.53	6.0%

Note: Fish *et al.*'s: Fish *et al.*'s blind deconvolution method;

New Conv. Crit.: method with new convergence criteria;

For each data set, both uniform and Gaussian initial estimates of PSF were used. In each case, both Fish's method and the method with new sub convergence criterion were studied.

Figures 5.19 and 5.20 presents the results on field data obtained from tube DHR009C015I010. The observed raw data is shown in figure 5.19 (a). The data after 3dB thresholding is shown in figure 5.19 (b). This raw data was then deconvolved using the Richardson – Lucy algorithm. Figures 5.19 (c) and (e) present the results obtained using a uniform initial estimate of PSF. Figures 5.19 (d) and (f) present the estimated PSF using a uniform initial estimate for PSF. Figures 5.20 (a) and (c) present the results obtained using a Gaussian initial estimate of PSF, and figures 5.20 (b) and (d) present the estimated PSF using a Gaussian initial estimate of PSF.

The results in both cases show that initial estimate for PSF has a big impact on the final results. The results obtained using Gaussian initial estimate for PSF is better than the results obtained using uniform initial estimate for PSF. Comparing the results obtained using Fish's method and the method with new convergence criteria, we can see that both methods perform well for this field data set. Although the method with new convergence criteria does not dramatically improve the final results, it offers savings on computational time.

Figures 5.21 and 5.22 presents the results on field data obtained from tube DHR006C012I010. The observed raw data is shown in figure 5.21 (a). The data after 3dB thresholding is shown in figure 5.21 (b). This raw data was then deconvolved using the Richardson – Lucy algorithm. Figures 5.21 (c) and (e) present the results obtained using a uniform initial estimate of PSF. Figures 5.21 (d) and (f) present the estimated PSF using a uniform initial estimate for PSF. Figures 5.22 (a) and (c) present the results obtained using a

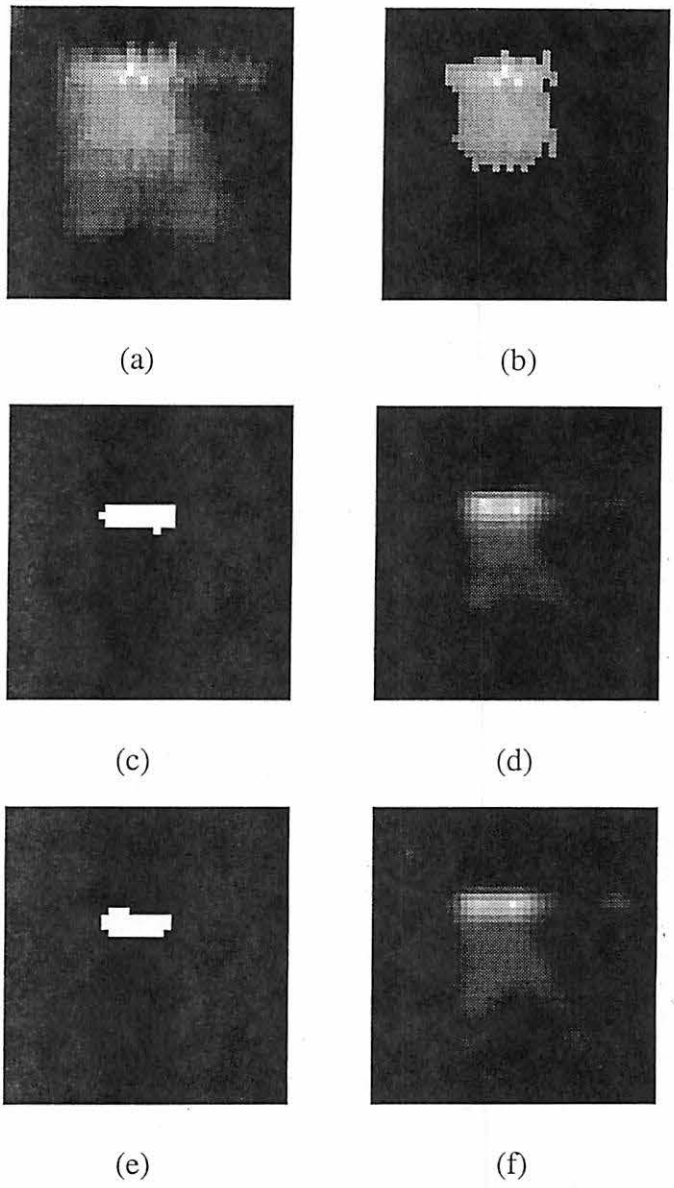

Figure 5.19 Results on a defect in tube No: DHR009C015I010, excitation frequency: 400 kHz; (a) Raw data; (b) Raw data after 3dB thresholding; (c) Deconvolved defect profile using uniform initial estimate of PSF (Fish, after 70 R – L iterations); (d) Estimated PSF using uniform initial estimate of PSF (Fish); (e) Deconvolved defect profile using uniform initial estimate of PSF (new convergence criteria, after 62 R – L iterations); (f) Estimated PSF using uniform initial estimate of PSF (new convergence criteria)

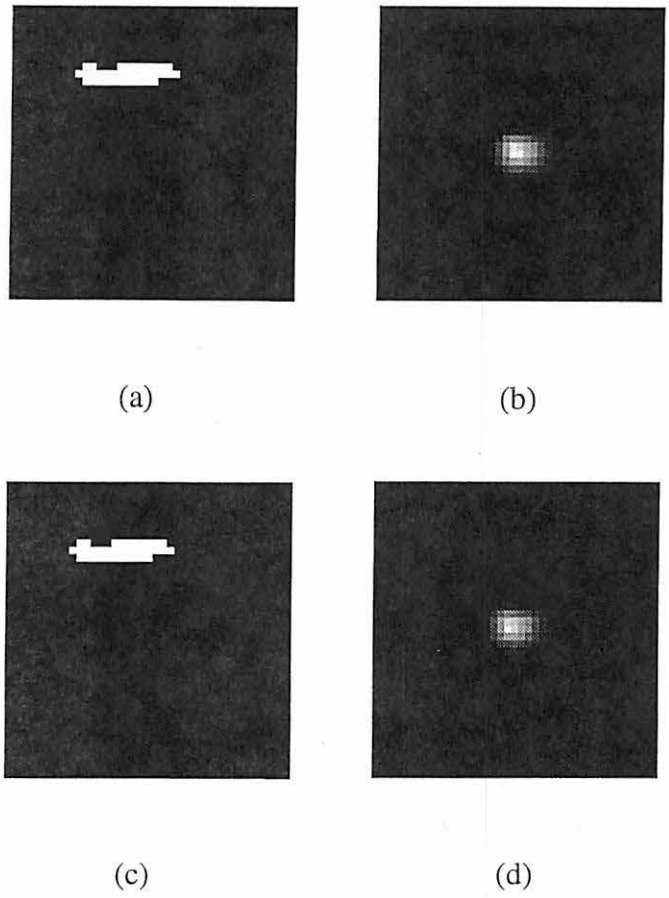

Figure 5.20 Results on a defect in tube No: DHR009C015I010, excitation frequency: 400 kHz; (a) Deconvolved defect profile using Gaussian initial estimate of PSF (Fish, after 60 R – L iterations); (b) Estimated PSF using Gaussian initial estimate of PSF (Fish); (c) Deconvolved defect profile using Gaussian initial estimate of PSF (new convergence criteria, after 52 R – L iterations); (d) Estimated PSF using Gaussian initial estimate of PSF (new convergence criteria)

Gaussian initial estimate of PSF, and figures 5.22 (b) and (d) present the estimated PSF using a Gaussian initial estimate of PSF.

The results in both cases show that initial estimate for PSF has a big impact on the final results. The results obtained using Gaussian initial estimate for PSF is better than the results obtained using uniform initial estimate for PSF. Comparing the results obtained using Fish's method and the method with new convergence criteria, we can see that both methods perform well for this field data set. Although the method with new convergence criteria does not dramatically improve the final results, it offers savings on computational time.

Figures 5.23 and 5.24 presents the results on field data obtained from tube DHR014C059I020. The observed raw data is shown in figure 5.23 (a). The data after 3dB thresholding is shown in figure 5.23 (b). This raw data was then deconvolved using the Richardson – Lucy algorithm. Figures 5.23 (c) and (e) present the results obtained using a uniform initial estimate of PSF. Figures 5.23 (d) and (f) present the estimated PSF using a uniform initial estimate for PSF. Figures 5.24 (a) and (c) present the results obtained using a Gaussian initial estimate of PSF, and figures 5.24 (b) and (d) present the estimated PSF using a Gaussian initial estimate of PSF.

The results in both cases show that initial estimate for PSF has big impact on the final results. The results obtained using Gaussian initial estimate for PSF is better than the results obtained using uniform initial estimate for PSF. Comparing the results obtained using Fish's method and the method with new convergence criteria, we can see that both methods perform well for this field data set. Although the method with new convergence criteria does not dramatically improve the final results, it offers savings on computational time.

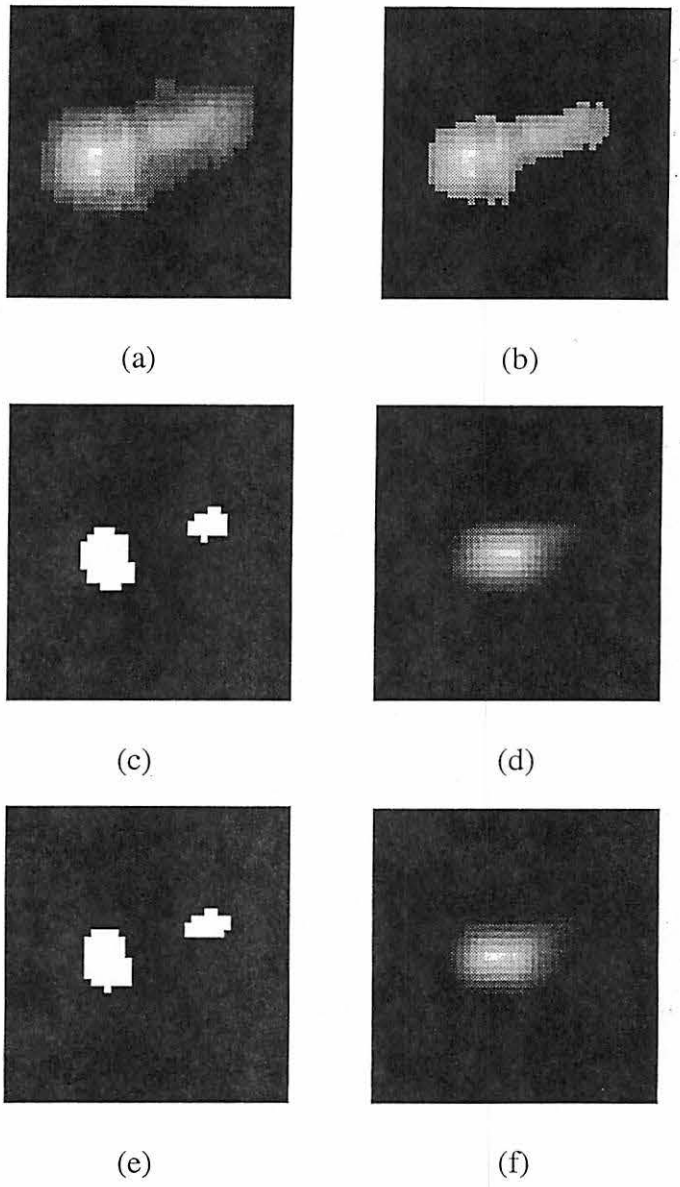

Figure 5.21 Results on a defect in tube No: DHR006C012I010, excitation frequency: 400 kHz; (a) Raw data; (b) Raw data after 3dB thresholding; (c) Deconvolved defect profile using uniform initial estimate of PSF (Fish, after 40 R – L iterations); (d) Estimated PSF using uniform initial estimate of PSF (Fish); (e) Deconvolved defect profile using uniform initial estimate of PSF (new convergence criteria, after 34 R – L iterations); (f) Estimated PSF using uniform initial estimate of PSF (new convergence criteria)

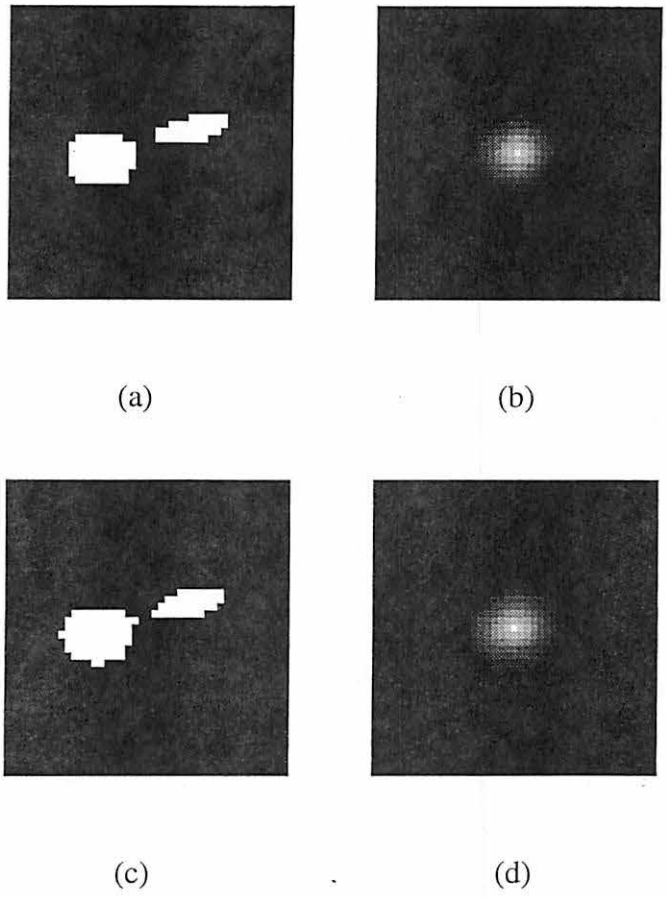

Figure 5.22 Results on a defect in tube No: DHR006C012I010, excitation frequency: 400 kHz; (a) Deconvolved defect profile using Gaussian initial estimate of PSF (Fish, after 40 R – L iterations); (b) Estimated PSF using Gaussian initial estimate of PSF (Fish); (c) Deconvolved defect profile using Gaussian initial estimate of PSF (new convergence criteria, after 32 R – L iterations); (d) Estimated PSF using Gaussian initial estimate of PSF (new convergence criteria)

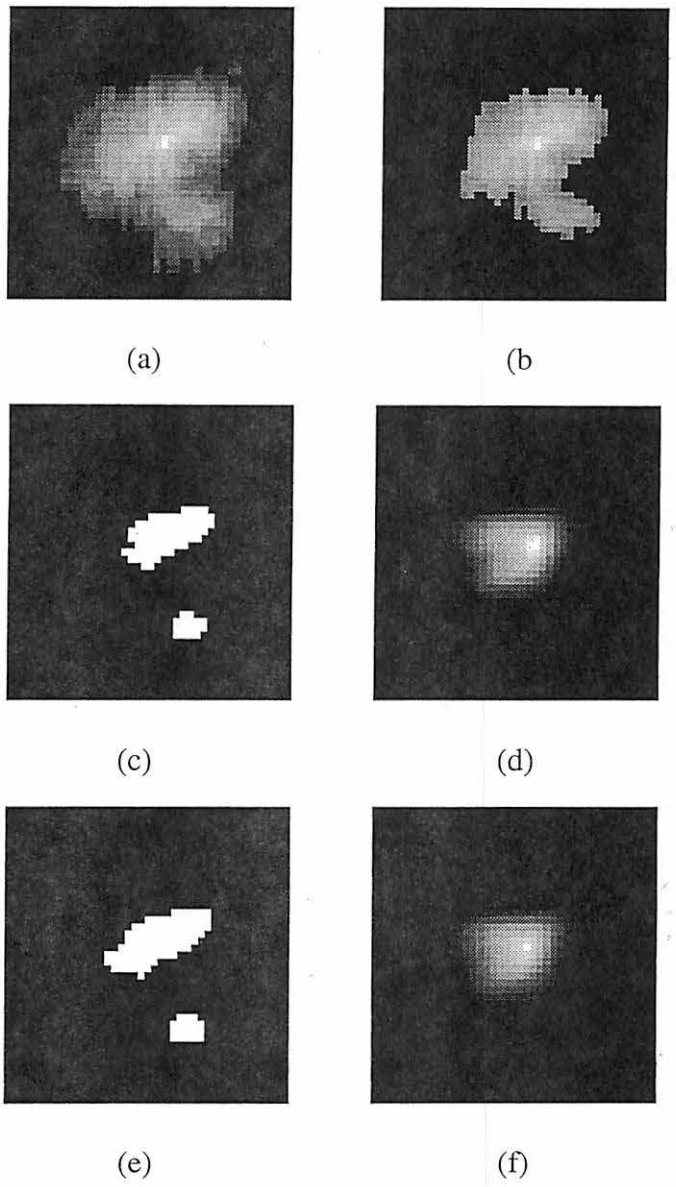

Figure 5.23 Results on a defect in tube No: DHR014C059I020, excitation frequency: 300 kHz; (a) Raw data; (b) Raw data after 3dB thresholding; (c) Deconvolved defect profile using uniform initial estimate of PSF (Fish, after 70 R – L iterations); (d) Estimated PSF using uniform initial estimate of PSF (Fish); (e) Deconvolved defect profile using uniform initial estimate of PSF (new convergence criteria, after 62 R – L iterations); (f) Estimated PSF using uniform initial estimate of PSF (new convergence criteria)

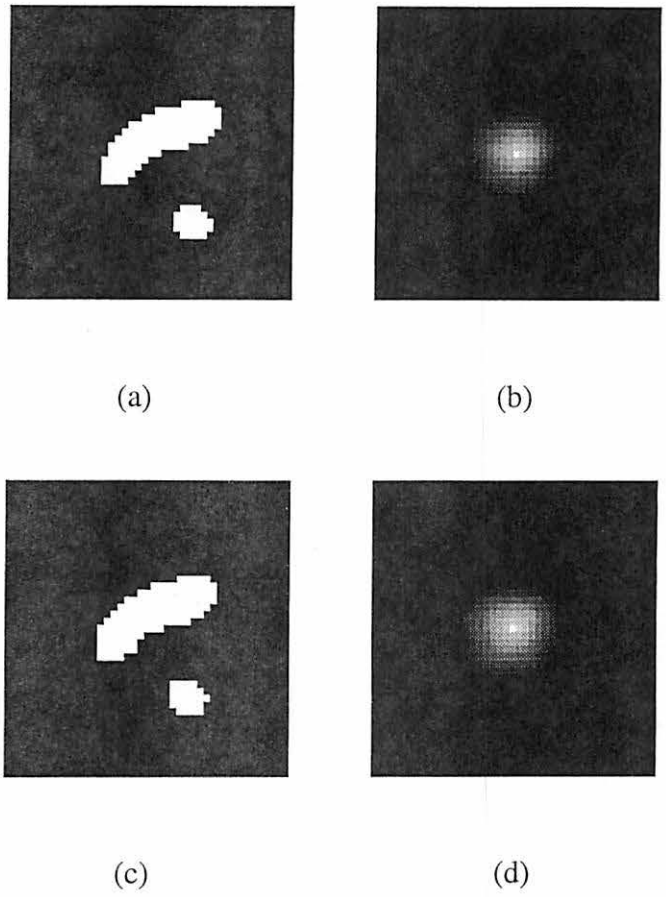

(a) (b)

(c) (d)

Figure 5.24 Results on a defect in tube No: DHR014C059I020, excitation frequency: 300 kHz; (a) Deconvolved defect profile using Gaussian initial estimate of PSF (Fish, after 40 R – L iterations); (b) Estimated PSF using Gaussian initial estimate of PSF (Fish); (c) Deconvolved defect profile using Gaussian initial estimate of PSF (new convergence criteria, after 36 R – L iterations); (d) Estimated PSF using Gaussian initial estimate of PSF (new convergence criteria)

5.2 Discussion

The data used to evaluate the blind deconvolution method based on Richardson – Lucy algorithm is obtained using rotating pancake probes. These probes operate in absolute mode. Another type of commonly used probe is the differential bobbin coil probe. This method does not perform well for the data obtained using bobbin coil. Since the Richardson – Lucy algorithm models probe impulse response as a probability density function, the probe impulse response has to possess the property of nonnegativity (shown in equation (4.6)). However the bobbin coil probe operates in differential mode, its response is usually a derivative of a Gaussian function. Therefore, the probe response does not satisfy the nonnegativity condition. For data obtained by using bobbin probe, other characterization methods, such neural networks, are more suitable.

5.2.1 Effect of Additive Noise

The inspection system model used does not take the additive noise into account. And the convergence criterion described in equation (4.23) ignores the noise as well. Hence this method may fail to converge when the level of additive noise is very high. Figures 5.25 - 5.28 show the results obtained by adding random noise of different SNR to test data set 2 (rectangle). From the results, it is clear that the method fails to achieve reasonable results when noise to signal ratio (NSR) is greater than 15%.

Although preprocessing techniques are used to remove noise, it is often very difficult to achieve a complete noise removal due the lack of knowledge of noise properties. Since the noise may be generated due to the vibration of the probe inside the tube, the friction between

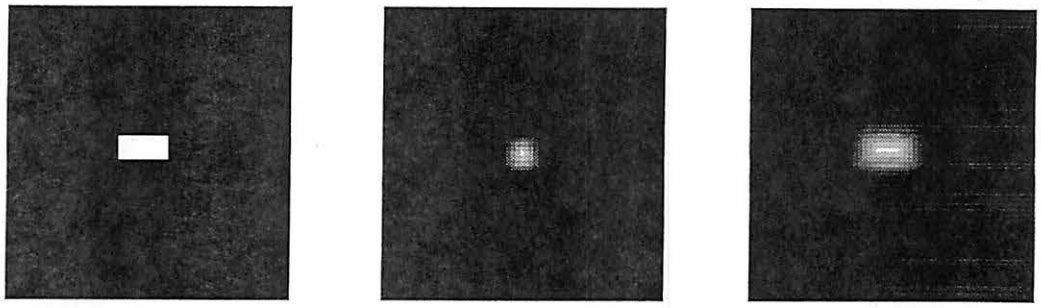

(a) (b) (c)

Figure 5.25 Test data set II. (a) True image; (b) Gaussian PSF; (c) Observed iamge.

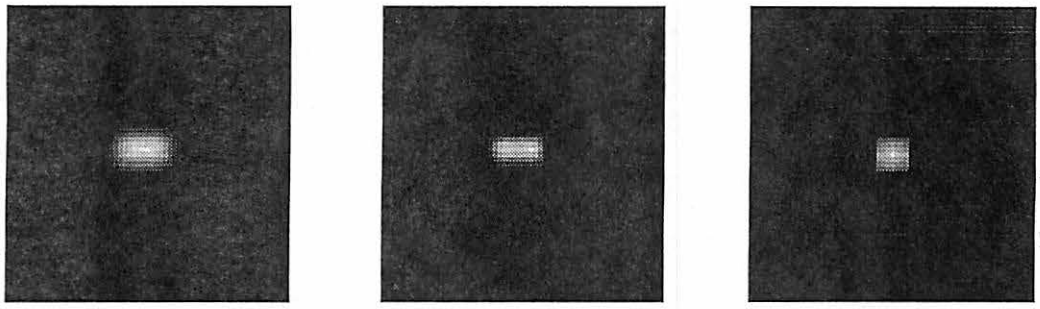

(a) (b) (c)

Figure 5.26 Results of test data set II (with 5% noise). (a) Observed image; (b) Deconvolved image; (c) Estimated PSF

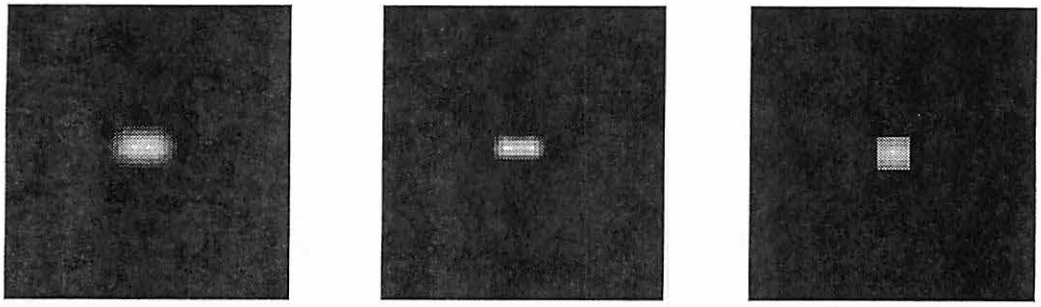

(a) (b) (c)

Figure 5.27 Results of test data set II (with 10% noise). (a) Observed image; (b) Deconvolved image; (c) Estimated SF

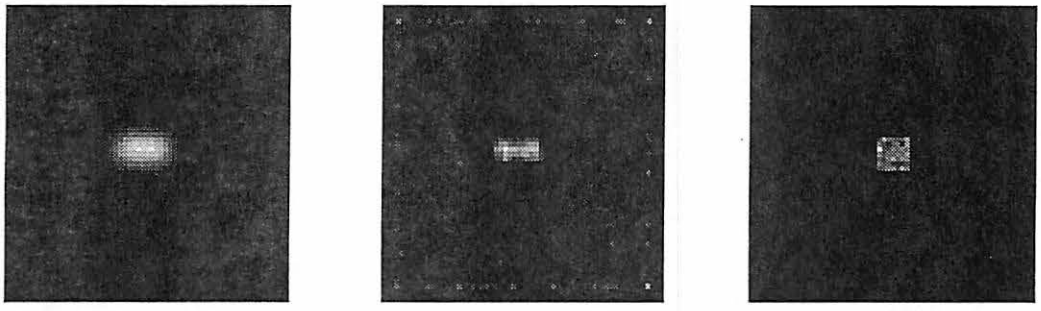

(a) (b) (c)

Figure 5.28 Results of test data set II (with 15% noise). (a) Observed image; (b) Deconvolved image; (c) Estimated PSF

the probe surface and the tube wall, the rust on the tube wall, and other reasons, it is very difficult to model the noise, and also it is almost impossible the estimate the statistical properties of the noise. Future research work in the area of the noise modeling will be useful. If the additive noise can be successfully modeled, then it can be removed more successfully, and can therefore dramatically improve the performance of this method.

5.2.2 Effect of Preprocessing

The primary objective of preprocessing is to remove the background noise of eddy current tube data so that the ROI of data can be obtained. Figure 5.29 and 5.30 show that the results of preprocessing for calibration data.

The results shows that the preprocessing can successfully remove background noise in the eddy current tube data while retain the information contained in the data.

5.2.3 Effect of Gaussian PSF

Blind deconvolution method based on Richardson – Lucy algorithm is sensitive to the initial estimate of PSF. Among three different initial estimates of PSF, Gaussian function performs best. And Gaussian functions with different σ value show almost the same results. Figure 5.31 - 5.34 present results on synthetic data using Gaussian functions with different σ value as the initial estimate of PSF. The "smearing" Gaussian PSF has σ value of 2.

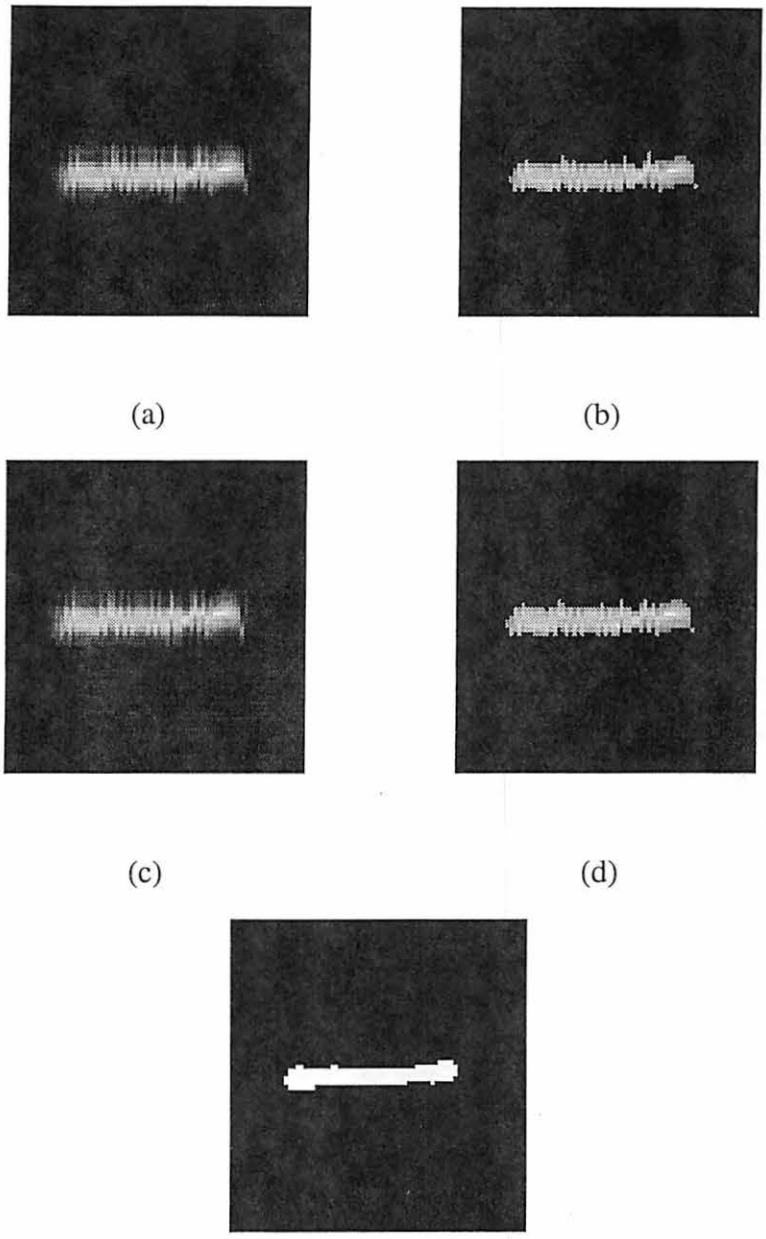

(a) (b)

(c) (d)

(e)

Figure 5.29 Results of Preprocessing on calibration data from defect A, excitation frequency 400 kHz. (a) raw data; (b) raw data after 3db thresholding; (c) data after preprocessing; (d) preprocessed data after 3db thresholding; (e) deconvolved defect profile

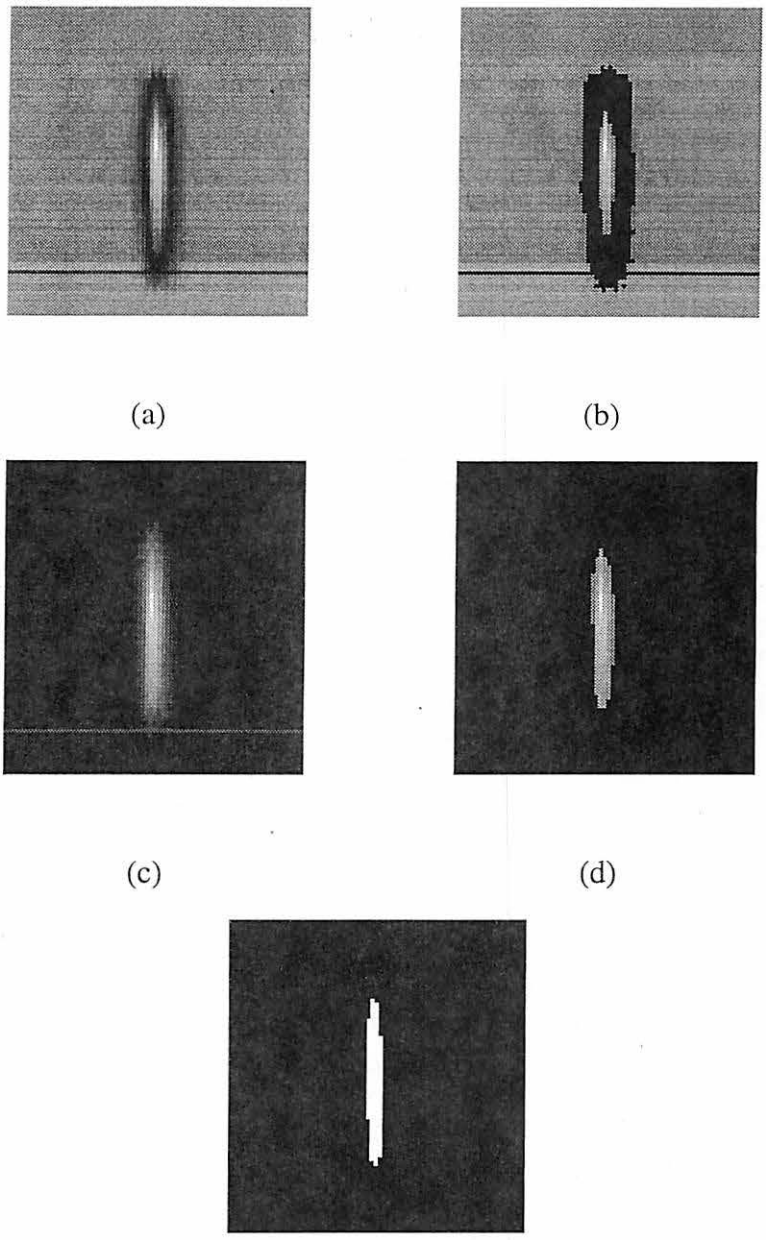

(a) (b)

(c) (d)

(e)

Figure 5.30 Results of Preprocessing on calibration data from defect E, excitation frequency 300 kHz. (a) raw data; (b) raw data after 3db thresholding; (c) data after preprocessing; (d) preprocessed data after 3db thresholding; (e) deconvolved defect profile

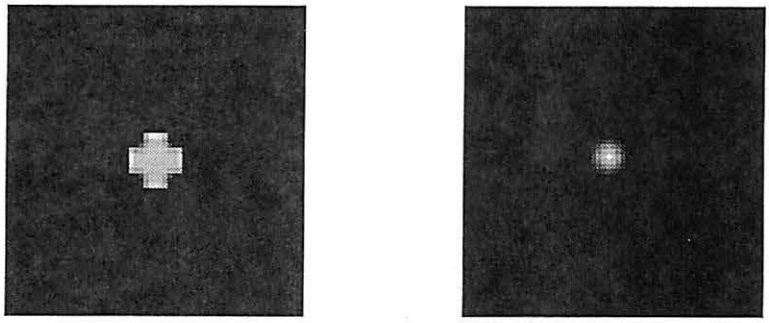

(a) (b)

Figure 5.31 Results on synthetic data set I using Gaussian initial estimate of PSF, $\sigma = 3$.

(a) Deconvolved image; (b) Estimated PSF;

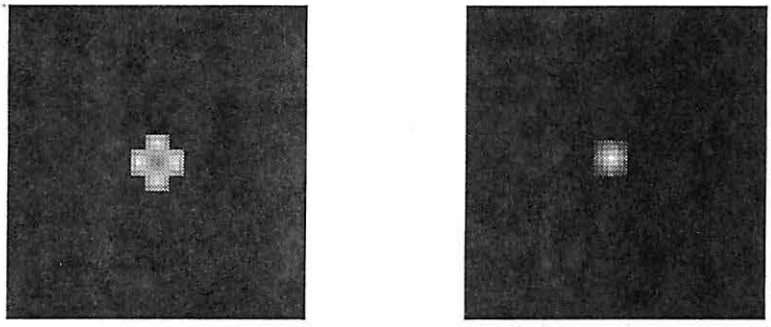

(a) (b)

Figure 5.32 Results on synthetic data set I using Gaussian initial estimate of PSF, $\sigma = 4$.

(a) Deconvolved image; (b) Estimated PSF;

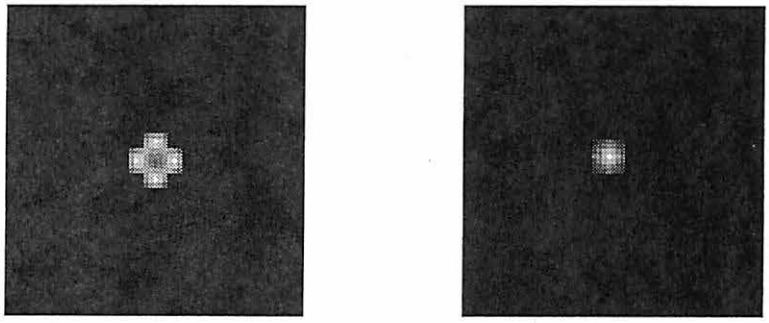

(a) (b)

Figure 5.33 Results on synthetic data set I using Gaussian initial estimate of PSF, $\sigma = 6$.

(a) Deconvolved image; (b) Estimated PSF;

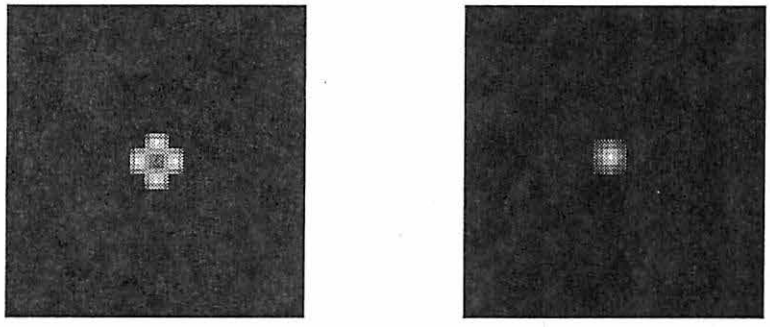

(a) (b)

Figure 5.34 Results on synthetic data set I using Gaussian initial estimate of PSF, $\sigma = 8$.

(a) Deconvolved image; (b) Estimated PSF;

5.3 Conclusion

The eddy current inspection problem is modeled as an image degradation system under the assumption that the observed eddy current data is the convolution of the true defect footprint and the probe impulse response. This makes it possible to apply blind deconvolution algorithms for signal restoration. Due to the nature of eddy current inspection process and the existence of additive noise, specific preprocessing steps for calibrating original data and removing noise are necessary. Since the scanning speed of rotating probe is not constant during the whole scanning process, another assumption made is that the probe impulse response remains unchanged in a local area in order to use the blind deconvolution algorithm. Iterative blind deconvolution method based on Richardson – Lucy algorithm was used in this application due to its properties of fast convergence and reasonable robustness. Initial results obtained show that blind deconvolution method based on Richardson – Lucy algorithm is capable of estimating the true defect footprint from eddy current data.

One major advantage of blind deconvolution method using Richardson – Lucy algorithm is that it converges very fast in comparison to other blind deconvolution methods. For all test data, results were obtained after a few iterations, typically after 3 to 8 iterations depending on the choice of the initial estimate for the probe PSF. The speed of convergence can be further improved by using the modified blind deconvolution method. This property is very important for steam generator tube inspection in nuclear power plant because of the large number of tubes to be inspected in a short period of time.

Besides fast convergence, the blind deconvolution method using Richardson – Lucy algorithm is also relatively robust. In the case where the additive noise level is low, the method performs very well. But at high noise levels, the method fails. Due to this problem,

when applying this method to eddy current data, preprocessing is necessary to get rid of a certain level of noise so that the blind deconvolution method can perform well.

Another issue that is worth mentioning is that the iterative blind deconvolution method is sensitive to the initial estimate of the true defect footprint and probe response. In the case that the true defect footprint and probe response are unknown, since for absolute pancake probe, response has the form of a Gaussian function, it is appropriate to use a 2 – dimensional Gaussian function as the initial estimate of the probe response. Comparison of the results obtained using data with both uniform and Gaussian function as the initial estimate of probe response show that the results obtained in the latter case are better. Another advantage of using data with Gaussian function as the initial estimate is that the method converges faster than with uniform function as the initial estimate. Considering the large number of tubes to be inspected in a practical application, this can greatly enhance the speed, reduce the cost, and improve the quality of service.

5.4 Future Research

The blind deconvolution method based on Richardson – Lucy algorithm is sensitive to the initial estimate of the defect footprint and probe response. Since no knowledge of defect footprint is available a priori, using a uniform distribution function is a reasonable solution. When choosing the initial estimate of probe response, a Gaussian distribution function is more suitable to model the probe response. Although the parameters of the Gaussian distribution can be estimated roughly from the sampling rate, the method can perform even better if the initial estimate of the probe response can be more accurate. This brings a possible future research area, namely probe response modeling using finite element model. In

the finite element model, all the information including lift off, geometry of the probe, conductivity and permeability of the material of the tube and coil, and the current density can be incorporated into the estimation process, thus more accurate estimate of the probe PSF can be achieved.

BIBLIOGRAPHY

[1] L. Udpa and W. Lord, "New approaches for multifrequency ECT of steam generator tubes", *Proc. of the ISMM Int. Symposium,* Honolulu (USA), February 1988, ACTA Press, pp.108-112

[2] M. R. Banham and A. K. Katsaggelos, "Digital image restoration," *IEEE Signal Proc. Magazine,* vol. 14, no. 2, pp. 24-41, March 1997.

[3] R. C. Gonzalez and R. E. Woods, *Digital Image Processing*, Addison-Wesley, Reading, MA, 1992.

[4] D. A. Fish, A. M. Brinicombe, E. R. Pike and J. G. Walker, "Blind deconvolution by means of the Richardson-Lucy algorithm," *J. Opt. Soc. Am. A,* vol. 12, no. 1, pp.58-65, January 1995.

[5] W. H. Richardson, "Bayesian-based iterative method of image restoration," *J. Opt. Soc. Am. A,* vol. 62, no. 1, pp.55-59, January 1972.

[6] L. B. Lucy, "An iterative technique for the rectification of observed distributions," *the Astronomical Journal*, vol. 79, no. 6, pp.745-754, June 1974

[7] L. Udpa, "Imaging of Electromagnetic NDT Phenomena." Ph. D. Dissertation, Colorado State University, Ft. Collins, 1985.

[8] D. E. Bray and R. K. Stanley, *Nondestructive Evaluation, a Tool for Design, Manufacturing, and Service*, McGraw – Hill Book Company, U.S.A, 1989.

[9] D. W. Fitting and L. Adler, *Ultrasonic Spectral Analysis for Nondestructive Testing*, Plenum Press, New York, 1981

[10] J. Sziland (Editor), *Ultrasonic Testing*, John Wiley & Sons, Ltd., New York, 1982.

[11] R. C. McMaster, P. Mcintire, and M. L. Mester(Editors), *Nondestructive Testing Handbook (volume 4): Electromagnetic Testing*, American Society for Nondestructive Testing, 1986

[12] D. J. Hagemajer, *Fundamental of Eddy Current Testing*, ASNT, Columbia, OH, 1990.

[13] R. S. Sharpe, *Research Techniques in Non – destructive Testing*, vol. VIII, Academic Press, London, 1985.

[14] D. Kundur and D. Hatzinakos, "Blind Image Deconvolution," *IEEE Signal Processing Mag.* Vol. 13, pp. 43 – 64, May, 1996.

[15] D. Kundur and D. Hatzinakos, "Blind Image Deconvolution Revisited," *IEEE Signal Processing Mag.* Vol. 13, pp. 61 – 64, November, 1996.

[16] M. R. Banham and A. K. Katsaggelos, "Digital Image Restoration," *IEEE Signal Processing Mag.* Vol. 14, pp. 24 – 41, 1997.

[17] A. K. Jain and S. Ranganath, "Applications of Two Dimensional Spectral Estimation in Image Restoration," *Proc. IEEE Int Conf Acoustics, Speech, Signal Processing*, pp. 1113 – 1116, 1981.

[18] B. R. Hunt, "The Application of Constrained Least Squares Estimation to Image Restoration by Digital Computer," IEEE Trans Comput, C – 22, pp. 805 – 812. September, 1973.

[19] A. O. Aboutalib and L. M. Sliverman, "Restoration of Motion Degraded Images," *IEEE Trans Cir Sys*, CAS – 22, pp. 278 –286, March, 1975

[20] J. Biemond, R. L. Lagendijk, and R. M. Mersereau, "Iterative Methods for Image Deblurring," *Proc IEEE*, vol. 78(5), pp. 856 – 883, May, 1990

[21] R. G. Lane and R. H. T. Bates, "Automatic Multidimensional Deconvolution," *J Opt Soc Am A*, vol. 4(1), pp. 180 – 188, January, 1987

[22] S. Haykin(editor), *Blind Deconvolution*, Prentice Hall, Englewood Cliffs, NJ, 1991.

[23] I. S. Stefanescu, "On the phase retrieval problem in two dimensions," *J Math Phys*, vol. 26, pp. 2141 – 2160, 1985.

[24] D. C. Ghiglia, L. A. Romero, and G. A. Mastin, "Systematic Approach to Two – dimensional Blind Deconvolution by Zero – Sheet Separation," *J Opt Soc Am A*, vol. 10(5), pp. 1024 – 1036, May, 1993.

[25] M. Cannon, "Blind Deconvolution of Spatially Invariant Image Blurs with Phase," *IEEE Trans Acoust, Speech, Signal Processing*, vol. 24(1), pp. 58 – 63, February, 1976.

[26] W. K. Pratt, "Vector Space Formulation of Two – dimensional Signal Processing Operations," *Comput. Graphics and Image Processing*, no. 4, pp. 1 – 24, 1975.

[27] R. L. Lagendijk, A. M. Tekalp, and J. Biemond, "Maximum Likelihood Image and Blur Identification: a Unifying Approach," *Optical Engineering*, vol. 29(5), pp. 422 – 435, May, 1990.

[28] R. L. Lagendijk, J. Biemond, and D. E. Boekee, "Identification and Restoration of Noisy Blurred Images Using the Expectation – Maximization Algorithm," *IEEE Trans Acoust, Speech, Signal Processing*, vol. 38(7), pp. 1180 – 1191, July, 1990.

[29] S. J. Reeves and R. M. Mersereau, "Blur Identification by the Method of Generalized Cross – Validation," *IEEE Trans Image Processing*, vol. 1(3), pp. 301 – 311, July, 1992.

[30] B. C. MaCallum, "Blind Deconvolution by Simulated Annealing," *Optics Communications*, vol. 75(2), pp. 101 – 105, February, 1990.

[31] D. Kundur, and D. Hatzinakos, "A Novel Blind Deconvolution Scheme for Image Restoration Using Recursive Filtering," *IEEE Trans Signal Processing*, vol. 46(2), pp. 372 – 390, February, 1998.

[32] C. A. Ong and J. A. Chambers, "An Enhanced NAS – RIF Algorithm for Blind Image Deconvolution," *IEEE Trans Image Processing*, vol. 8(7), pp. 988 – 992, July, 1999.

[33] G. R. Ayers and J. C. Dainty, "Iterative Blind Deconvolution Method and Its Applications," *Optics Letters*, vol. 13(7), pp. 547 – 549, July, 1988.

[34] B. L. Davey, R. G. Lane, and R. H. T. Bates, "Blind Deconvolution of a Noisy Complex – Valued Image," *Optics Communications*, vol. 69(5,6), pp. 353 – 356, January, 1989.

[35] N. Miura, N. Baba, S. Isobe, M. Noguchi, and Y. Norimoto, "Binary Star Reconstruction with Use of the Blind Deconvolution Method," *Journal of Modern Optics*, vol. 39(5), pp. 1137 – 1146, May, 1992.

[36] F. Tsumuraya, N. Miura, and N. Baba, "Iterative Blind Deconvolution Method Using Lucy's Algorithm," *Astron Astrphys*, vol. 282(2), pp. 699 – 708, February, 1994.

[37] S. Kirkpatrick, C. D. Gelatt Jr., and M. P. Vecchi, "Optimization by Simulated Annealing," *Science*, vol. 220, pp. 671 – 680, 1983.

[38] R. A. Wiggins, "Minimum Entropy Deconvolution," *Geoexploration*, vol. 16, pp. 21 – 35, 1978.

[39] H. S. Wu, "Minimum Entropy Deconvolution for Restoration of Blurred Two – tone Images," *Electronics Letters*, vol. 26(15), pp. 1183 – 1184, July, 1990.

[40] G. Jacovitti and A. Neri, "A Bayesian Approach to 2D Non Minimum Phase AR Identification," *Fifth ASSP Workshop on Spectrum Estimation and Modelling*, pp. 79 – 83, 1990.

[41] T. J. Holmes, "Blind Deconvolution of Quantum – limited Incoherent Imagery: Maximum Likelihood Approach." *J. Opt. Soc. Am.*, A 9, pp. 1052 – 1061, 1992.

[42] M. Ali, "3 – D Characterization of Eddy Current NDE Signal", M. S. thesis, Iowa State University, 1999